EDGE ARTICLE

Check for updates

Engineering intraporous solvent environments: effects of aqueous-organic solvent mixtures on competition between zeolite-catalyzed epoxidation and H$_2$O$_2$ decomposition pathways†

David S. Potts, [ID] Chris Torres, Ohsung Kwon and David W. Flaherty*

Solvent molecules alter the free energies of liquid phase species and adsorbed intermediates during catalytic reactions, thereby impacting rates and selectivities. Here, we examine these effects through the epoxidation of 1-hexene (C$_6$H$_{12}$) with hydrogen peroxide (H$_2$O$_2$) over hydrophilic and hydrophobic Ti-BEA zeolites immersed in aqueous solvent mixtures (acetonitrile, methanol, and γ-butyrolactone). Greater H$_2$O mole fractions provide greater epoxidation rates, lower H$_2$O$_2$ decomposition rates, and hence improved H$_2$O$_2$ selectivities to the desired epoxide product in each combination of solvent and zeolite. The mechanisms for epoxidation and H$_2$O$_2$ decomposition remain constant across solvent compositions; however, H$_2$O$_2$ activates reversibly in protic solutions. Differences in rates and selectivities reflect the disproportionate stabilization of transition states within zeolite pores with respect to surface intermediates and fluid phase reactants, as evinced by turnover rates normalized by the activity coefficients of C$_6$H$_{12}$ and H$_2$O$_2$. Opposing trends in activation barriers suggest that the hydrophobic epoxidation transition state disrupts hydrogen bonds with solvent molecules, while the hydrophilic decomposition transition state forms hydrogen bonds with surrounding solvent molecules. Solvent compositions and adsorption volumes within pores, from ^{1}H NMR spectroscopy and vapor adsorption, depend on the composition of the bulk solution and the density of silanol defects within pores. Strong correlations between epoxidation activation enthalpies and epoxide adsorption enthalpies from isothermal titration calorimetry indicate that the reorganization of solvent molecules (and associated entropy gains) required to accommodate transition states provides the most significant contribution to the stability of transition states that determine rates and selectivities. These results demonstrate that replacing a portion of organic solvents with H$_2$O offers opportunities to increase rates and selectivities for zeolite-catalyzed reactions while reducing usage of organic solvents for chemical manufacturing.

1. Introduction

Epoxides are used as intermediates to manufacture fragrances, plastics, and biologically active ingredients and are produced and consumed on a massive scale.[1] The primary methods to produce epoxides industrially include the chlorohydrin process, organic-hydroperoxide (Halcon) process, and hydrogen peroxide (H$_2$O$_2$) to propylene oxide (HPPO) process.[1] Industrial HPPO processes involve one of two combinations of a microporous titanosilicate catalyst and an aqueous organic solvent: Ti-MFI (*i.e.*, titanosilicate-1) with aqueous methanol (CH$_3$OH)[2,3] or Ti-MWW with aqueous acetonitrile (CH$_3$CN).[3–7] The reactant streams for these processes often include aqueous H$_2$O$_2$, which

introduces a mole fraction of water (x_{H_2O}) reported in the range of 0.05 to 0.3;[2,3,5,6] however, patented processes add water (H$_2$O) to the reaction mixture even when producing H$_2$O$_2$ *in situ* from H$_2$ and O$_2$.[3,4,7] These reports imply that H$_2$O may improve epoxidation performance, but the reasons for these differences and the magnitude of the effects are not reported.[2–7]

The quantity of H$_2$O combined with organic solvents in binary, ternary, or more complex solvents affects rates of catalytic reactions. For example, turnover rates for homogeneous Brønsted acid-catalyzed alcohol dehydrations increase by two to three orders of magnitude when changing the solvent from neat H$_2$O to mixtures of H$_2$O and organic solvents (*i.e.*, >0.3 molar fraction of dimethyl sulfoxide, dioxane, tetrahydrofuran (THF), CH$_3$CN, or gamma-valerolactone).[8–10] A separate work revealed that furfuryl acid hydrolysis yields over Brønsted acidic zeolite H-MFI increased from less than 10% in neat H$_2$O to nearly 70% in an equimolar THF–H$_2$O mixture.[11] Authors of these studies attribute rate changes to differences in the solvent environment

Department of Chemical and Biomolecular Engineering, University of Illinois Urbana-Champaign, Urbana, IL 61801, USA. E-mail: dwflhrty@illinois.edu

† Electronic supplementary information (ESI) available. See DOI: https://doi.org/10.1039/d2sc06473a

around the reactant in the fluid phase or within the zeolite pores as the solvent composition varies. Solvent molecules interact with and alter the stability of reactive species, which can influence rates of homogeneous and heterogeneous catalytic reactions.[12–16]

Within the field of organocatalysis, recent studies sought to manipulate the rates and selectivities achieved by catalytic complexes by tailoring outer-sphere interactions, also known as second coordination sphere effects.[17,18] Outer-sphere interactions encompass hydrogen bonding, electrostatic, and hydrophobic interactions, among others. These interactions may be manipulated through alterations to the ligand structure and ion pairs but also by changes to the composition of the solvent.[19] Researchers have long appreciated that solvents influence enzymatic[20] and organocatalytic[21] reactions, with publications dating to 1890 showing that the solvent choice altered rates for the quaternization of triethylamine with iodoethane by nearly 3 orders of magnitude.[22] Classical theories (e.g., Kirkwood,[23] Debye and Hückel,[24] and Kamlet and Taft[25]) provide frameworks to understand the influence of solvents on reaction rates by correlating bulk solvent properties to the thermodynamic activity of reactive intermediates (i.e., solutes). These descriptions rely on mean-field descriptions and do not describe phenomena at a molecular level. For these reasons, they cannot account for outer-sphere or solvent-mediated interactions at solid–liquid interfaces. Recently, we described a conceptual framework[14] for quantifying these effects within rate expressions for chemical reactions that captures the impact of solvent mediated interactions on the stability of reactive species

through excess free energy contributions (G^{ε}) (Scheme 1). These contributions arise from thermodynamic non-idealities that alter the activity coefficients of reactive species.[26] The non-idealities brought about by solvent molecules are functionally identical to second coordination sphere effects considered for homogeneous, enzymatic, and electrochemical catalytic processes.

Interactions between solvents and reactants at solid–liquid interfaces provide energetic contributions that strongly influence zeolite-catalyzed epoxidation reactions,[27–34] among other chemistries. For example, the identity of the organic solvent affects alkene epoxidation turnover rates. Previous work from our group and others showed that CH_3OH solvent gives greater epoxidation turnover rates for C_6–C_{18} linear and cyclic alkenes than CH_3CN over Ti-MFI,[29,35–37] but lower rates than CH_3CN over Ti-BEA[29,37–39] and Ti-MWW.[37,40,41] These differences reflect either direct effects of the zeolite topology or inadvertent or unrecognized effects that may include differences related to the densities of silanol defects (($SiOH)_x$, where x ranges from 1 to 4 and depends upon the mechanism of defect formation), variations in the crystal habit, particle dimensions, and associated intraparticle transport effects caused by variations in the synthesis protocol. Notably, the density of ($SiOH)_x$ impacts the hydrophilicity of the pores and the kinetics of liquid phase alkene epoxidations. Turnover rates for epoxidations of C_6–C_{18} linear alkenes in CH_3CN with aqueous H_2O_2 in hydrophilic Ti-BEA surpass rates in hydrophobic Ti-BEA by factors of 40 to 450.[27,33,34] The most hydrophilic zeolites possess multiple ($SiOH)_x$ nests per unit cell that stabilize hydrogen bonded networks of H_2O molecules within their pores, while the most hydrophobic zeolites contain far less than one ($SiOH)_x$ per unit cell and contain less H_2O.[42,43] During epoxidation turnovers, the formation of the alkene epoxidation transition state (or the adsorption of an epoxide) disrupts and displaces hydrogen bonded H_2O and CH_3CN molecules from pores and brings entropic gains that stabilize the transition state to increase rates.[27,34] In general, solvent molecules alter rates and activation free energies for catalytic reactions through changes in G^{ε} (Scheme 1).

Recent literature indicates that the presence of H_2O influences rates of alkene epoxidation; however, discrepancies among reports regarding the magnitude of these effects, the values of x_{H_2O} needed, differences between organic solvents, and disagreement over the physical origins motivate closer examination of these phenomena across common aqueous organic solvent mixtures. A fraction of studies showed that increasing x_{H_2O} does not affect rates for alkene epoxidations. Ramachandran et al. reported that 1-hexene (C_6H_{12})[35] epoxidation rates do not depend on x_{H_2O} ($0.03 \leq x_{H_2O} \leq 0.3$) and argued that H_2O does not enter pores or reside near Ti active sites. Bregante et al. showed that 1-octene (C_8H_{16}) epoxidation rates did not change with x_{H_2O} ($0.0002 \leq x_{H_2O} \leq 0.008$) and reasoned that the intrapore H_2O concentration remains constant in this dilute limit.[27] Other reports found that adding H_2O increases epoxidation rates of propylene (C_3H_6)[40] and C_6H_{12}.[37,39] The rate increases for each C_6H_{12} epoxidation study were attributed to the stabilization of titanium-hydroperoxo
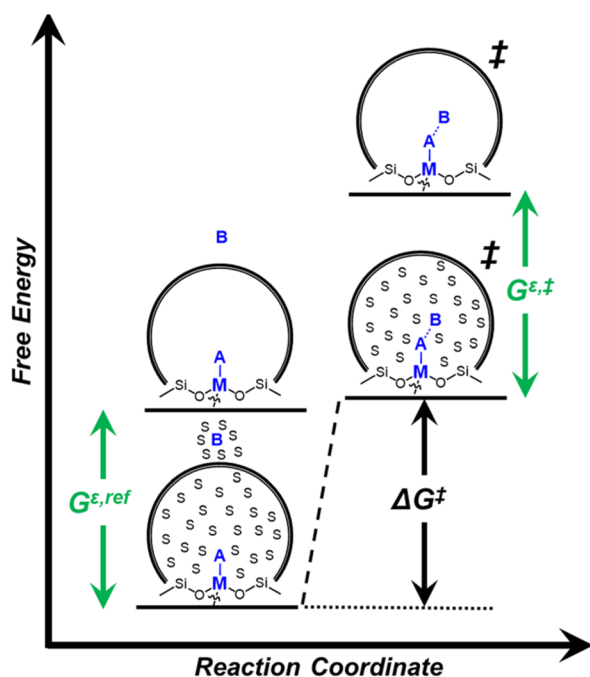
Scheme 1 Reaction coordinate depicting the influence of solvent molecules on a generic reaction over a metal (M)-incorporated zeolite between A and B through changes in the excess free energy of the reference state ($G^{\varepsilon,ref}$) and transition state ($G^{\varepsilon,\ddagger}$).

(Ti–OOH) reactive intermediates by the formation of a 5-membered ring with an H_2O molecule.[37,39] The ratio of the organic solvent (CH_3CN) to H_2O was proposed to affect rates by changing the hydrophilicity of the environment around Ti sites, which affected the access of C_3H_6 and H_2O_2 to Ti sites.[40] Rates and barriers for H_2O_2 decomposition (an undesirable side reaction) also depend on the choice of organic solvent used in aqueous mixtures,[39,44] however, the dependence upon x_{H_2O} has not been reported. Notably, these prior studies utilized different combinations of organic solvents (*e.g.*, CH_3OH, CH_3CN, acetone), Ti-zeolites (*i.e.*, *BEA, MFI, MWW frameworks), and reaction conditions (*i.e.*, temperature, reactant, and H_2O concentrations). Furthermore, reactant concentrations varied in ways that apparently yielded distinct kinetic regimes. Finally, speculative interpretations were rarely corroborated by complementary experimental methods to confirm the influence of x_{H_2O} on rates. Consequently, intentional pairing of solvents with surfaces for new systems of reactants, solvents, and catalysts relies on guesswork and experimentation. Solvent composition clearly influences the kinetics and possibly the mechanism for alkene epoxidation and H_2O_2 decomposition reactions at solid–liquid interfaces, underscoring the importance of understanding how x_{H_2O} influences epoxidation and H_2O_2 decomposition pathways.

Here, the interpretations of differences between the intrinsic kinetics for C_6H_{12} epoxidation and H_2O_2 decomposition reactions in aqueous-organic solvent environments within Ti-BEA zeolites show that solvation effects primarily govern rates and barriers. These comparisons control for potential variations in zeolite framework and reaction conditions that differed among previous studies, strengthening conclusions that solvent structures interact with adsorbed and liquid phase reactive species to influence catalysis. Turnover rates for C_6H_{12} epoxidation with aqueous H_2O_2 increase with x_{H_2O} ($0.002 \leq x_{H_2O} \leq 0.8$) while turnover rates for H_2O_2 decomposition decrease over hydrophilic (Ti-BEA-OH) and hydrophobic (Ti-BEA-F) zeolites in aqueous mixtures of three organic solvents (CH_3CN, CH_3OH, and γ-butyrolactone (GBL, $C_4H_6O_2$)). These trends result in greater epoxide formation rates and H_2O_2 selectivities at higher x_{H_2O}, regardless of the identity of the organic component of the solvent. Comparisons among turnover rates normalized by the solvent-dependent activity coefficients of the fluid phase reactants demonstrate that the solvent composition strongly influences the stability of intermediates and transition states within the pores of Ti-BEA. The interpretation of measured activation enthalpies and entropies for epoxidation and H_2O_2 decomposition shows that epoxidation rates rise with higher x_{H_2O} due to a combination of increased thermodynamic activity of fluid phase C_6H_{12} and increases in the entropy of the epoxidation transition state by the disruption of hydrogen bonds among intrapore H_2O molecules. In contrast, H_2O molecules likely enthalpically stabilize the hydrophilic transition state for H_2O_2 decomposition through hydrogen bonding but more significantly stabilize fluid phase H_2O_2 and Ti–OOH, leading to lower decomposition rates at higher x_{H_2O}. These interpretations agree with differences among 1,2-epoxyhexane adsorption enthalpies measured by isothermal titration calorimetry as functions of

solvent composition. Analysis of the activation barriers for both reaction pathways and the trends in epoxide adsorption enthalpies show that multiple kinetic and thermodynamic parameters depend sensitively on the values of x_{H_2O} and vary more significantly with x_{H_2O} in Ti-BEA-OH than Ti-BEA-F. These comparisons agree with differences among intrapore solvent compositions between zeolites and organic solvents, which show that $(SiOH)_x$ nests facilitate preferential uptake of H_2O within pores and lead to greater interaction among H_2O molecules and surface intermediates at any given x_{H_2O} for the bulk fluid. Cumulatively, these findings show how the stability of reactive intermediates and transition states for epoxidation vary due to interactions with intrapore H_2O molecules and demonstrate the ubiquity of these effects across solvent mixtures and zeolites with distinct hydrophilic or hydrophobic nature.

2. Materials and methods

2.1 Catalyst synthesis

Ti-BEA-OH was prepared by post-synthetic modification of commercial Al-BEA, following previously published procedures.[45,46] Al-BEA (TOSOH, lot no. 94HA6X02Y; Si : Al = 20) was treated in refluxing HNO_3 (Macron Chemicals, 68–70 wt%, 20 cm^3 g^{-1}) at 433 K for ~24 h to remove Al atoms from the *BEA framework by forming soluble $Al(NO_3)_3$. The dealumination treatment was carried out 3 times to ensure thorough dealumination (Si : Al > 1200). Between dealumination, the *BEA sample was washed with deionized H_2O (18.2 MΩ cm, Elga Purelab Flex 2, 50 cm^3 $g_{zeolite}^{-1}$) and recovered by vacuum filtration. After the last dealumination, the dealuminated *BEA was heated to 823 K (5 K min^{-1}) in flowing air (200 cm^3 min^{-1}; Airgas, Ultra Zero grade) and held at 823 K for 6 h to remove organic residues. The resulting material (Si-BEA-OH) was heated in a round-bottom flask under vacuum (<5 Pa, 473 K) to create a moisture-free environment, after which dichloromethane (CH_2Cl_2, Fisher Chemicals, 20 cm^3 $g_{zeolite}^{-1}$) solvent was added to the flask. Titanium atoms were then incorporated into the framework by adding $TiCl_4$ to the Si-BEA-OH and CH_2Cl_2 mixture under an inert atmosphere (328 K, refluxing CH_2Cl_2, ~16 h, 50 cm^3 min^{-1} Ar, Airgas, Ultra High Purity). The resulting Ti-BEA-OH was recovered by rotary evaporation and was heated to 823 K (5 K min^{-1}) in flowing air (200 cm^3 min^{-1}) and held at 823 K for 6 h, resulting in a white powder sample.

Ti-BEA-F was synthesized by following a previous procedure.[47,48] 16.82 g of tetraethylammonium fluoride hydrate (TEAF, Sigma-Aldrich, 98%) was dissolved in 27 cm^3 of deionized H_2O (18.2 MΩ cm, Elga Purelab Flex 2) in a polypropylene container. 39.87 cm^3 of tetraethylorthosilicate (TEOS, Sigma-Aldrich, >98 wt%) was added, and the mixture was stirred for 30 min at room temperature. 0.351 cm^3 of titanium(ɪᴠ) isopropoxide (TIPO, Sigma-Aldrich, 99.999%) was added, and the solution was covered and stirred for an additional 16 h to produce a white, opaque homogeneous solution. The cover was removed, and the mixture was stirred for 12 h to evaporate the alcohols formed from the hydrolysis of TIPO (isopropanol) and TEOS (ethanol). The mass of alcohols formed was estimated by assuming complete and stoichiometric hydrolysis of all TIPO and TEOS

added. The solution was left uncovered to allow the alcohols to evaporate until the mass of the solution decreased by an amount equal to 115% of the calculated mass of the alcohols to increase the likelihood of complete evaporation of these alcohols. The alcohols are assumed to evaporate preferentially before water based on their greater volatility. A mass of deionized H_2O equivalent to the difference between the total mass evaporated (36.8 g) and the calculated mass of alcohols formed (31.0 g) was added to account for the H_2O lost during evaporation. The mixture was then transferred to a Teflon liner (Parr Instruments, 125 cm^3, Model 4748). This yielded a gel with an approximate molar composition of $1Si : 0.006Ti : 0.56TEAF : 8.89H_2O$. A small amount of Si-BEA-OH seeds (3% by mass relative to SiO_2 in the synthesis gel) from a previous synthesis was added to promote crystallization. The Teflon liner was loaded into a stainless-steel autoclave (Parr Instruments, 125 cm^3, Model 4748) and heated to 413 K at dynamic conditions (60 rpm) in a convection oven (Yamato, DKN602C) for 20 days. The resulting material was recovered by centrifugation, washed with H_2O, and dried in an oven for 12 h at 343 K. The dried solid was heated at 5 K min^{-1} to 823 K in flowing air (200 cm^3 min^{-1}) and held at 823 K for 6 h to produce a white powder Ti-BEA-F sample.

2.2 Catalyst characterization

The titanium (Ti), silicon (Si), and aluminum (Al) contents of the Ti-BEA catalysts were determined with energy-dispersive X-ray fluorescence (EDXRF). Finely ground samples of Ti-BEA ($\sim$50 mg) were loaded into a polypropylene cup (1 cm diameter) sealed with ultralene film. The sample cups were loaded into the He-purged chamber of the spectrometer (Shimadzu, EDX-7000). The samples were scanned between 0 and 30 keV, and the intensities of the fluorescence features were used to calculate the mass of Ti, Si, and Al within the sample. The EDXRF measurements show that Ti-BEA-OH (Si : Al $\sim$ 1200) and Ti-BEA-F (Si : Al $\sim$ 1750) contain only trace quantities of Al. The trace amount of Al in Ti-BEA-F may result from Al impurities from the components used in the synthesis. Compositions of the Ti-BEA samples were also assessed by ICP-OES, which confirmed each sample contained negligible quantities of Al (Si : Al > 2800) and possessed Ti quantities consistent with the results from EDXRF. Ti loadings and Si : Al ratios for each zeolite are shown in Table 1.

The dispersity of the Ti atoms in the Ti-BEA catalysts was measured with diffuse reflectance UV-vis (DRUV-vis) spectroscopy. Magnesium oxide (MgO, Sigma-Aldrich, 99.9995%) was used as a background. Ti-BEA samples were mixed and ground into a fine powder with magnesium oxide at a MgO : Ti-BEA mass ratio of 10 : 1 to measure sample spectra on a UV-vis spectrophotometer (Varian, Cary 5G). The total reflectance spectra were measured under ambient conditions, and the band gap energies (Table 1) were determined by extrapolating the linear portion of the Tauc plots to the horizontal axis to determine the minimum energy of photons absorbed (eV) (Fig. S1†).

The crystallinities of the Ti-BEA samples were confirmed using an X-ray diffractometer (Bruker, D8 Advance) with Cu Kα radiation under ambient conditions. The Ti-BEA samples were ground into a fine powder and loaded into a polypropylene sample holder for the measurements. The diffractograms of the Ti-BEA samples match previously reported powder diffraction patterns for zeolite *BEA (Fig. S2†).[49] These diffractograms confirm that all Ti-BEA samples possess the *BEA zeolite framework. Anatase TiO_2 contains a strong feature at $\sim$25.5°,[50] while the *BEA framework shows a weak feature in the same location. The patterns for each Ti-BEA and Si-BEA-OH in Fig. S2† possess a small feature in this region, suggesting that the feature either originates from a *BEA framework feature or minimal quantities of TiO_2 present within the Ti-BEA materials.

Ex situ Raman spectra of the Ti-BEA catalysts were measured with a Raman spectrometer (Renishaw, InVia) equipped with a 532 nm laser. The measurements were performed at ambient conditions on pressed catalyst pellets. The accumulation time was 20 s per scan, and each Raman spectra was calculated by averaging 10 scans. The delivered power density was approximately 2 mW μm^{-2}, as measured by a power meter (Gentec-EO, PRONTO-SI). The Raman spectra for each Ti-BEA (Fig. S3†) lack discernible features at 144 cm^{-1}, which indicates the absence of Ti–O–Ti bonds present in anatase TiO_2. In conjunction with the high band gaps (4.3 eV, Table 1) of these materials and the absence of strong TiO_2 features on the XRD patterns, these spectra indicate that Ti atoms reside in tetrahedral positions within the *BEA framework.

The surface area and micropore volumes of each Ti-BEA were determined using gas-phase adsorption isotherms of N_2 (77 K) and Ar (87 K). The effect of $(SiOH)_x$ density on gaseous solvent uptake was determined from adsorption isotherms of H_2O and CH_3OH (295 K). All adsorption isotherms were collected on a volumetric adsorption instrument (Micromeritics, 3Flex). The Ti-BEA samples were pelletized and sieved to retain particles from 100–250 μm in diameter. The samples were degassed under dynamic vacuum prior to adsorption (<7 × 10^{-4} Pa, 673 K, 3 h). The surface area was calculated using the Rouquerol-

Table 1 Ti Content, Band Gap, and Relative Hydrophilicity of Synthesized Ti-BEA

Catalyst	Si : Al	Ti wt%	Band gap[c] (eV)	Φ_{IR}[d]	BET surface area[e] (m^2 g^{-1})	Micropore volume[f] (cm^3 g^{-1})
Ti-BEA-OH	1220[a], 2800[b]	0.36[a], 0.34[b]	4.3	2.25	628	0.172
Ti-BEA-F	1750[a], 2880[b]	0.26[a], 0.25[b]	4.3	0.27	543	0.173

[a] Determined with EDXRF. [b] Measured with ICP. [c] Extracted from leading edge of Tauc plot from DRUV-vis. [d] Calculated from infrared transmission spectra of dehydrated Ti-BEA samples. [e] Measured by volumetric Ar physisorption. [f] Calculated using the t-plots from Ar physisorption.

modified Brunauer–Emmett–Teller (BET) method,[51] and the micropore volume was determined from the t-plot method.[52] Fig. S4† shows the N_2 and Ar isotherms, and Table S1† presents the total and external surface area, BET surface area and pore volume from N_2 adsorption, and total pore volume for each Ti-BEA. The H_2O and CH_3OH isotherms are displayed in Fig. S5.†

The relative density of $(SiOH)_x$ groups within the Ti-BEA catalysts was measured using infrared spectroscopy. Catalyst pellets (~50 mg) were loaded into a transmission cell configured with CaF_2 windows. The transmission cell was connected to a temperature controller and gas manifold, then loaded into a Fourier-transform infrared spectrometer (Bruker, Vertex 70) equipped with a liquid N_2-cooled HgCdTe detector, as described previously.[53] The cell was first heated to 573 K at ~5 K min^{-1} and held for 2 hours in flowing He (50 cm^3 min^{-1}, 99.997%, Airgas) to desorb any water and volatile compounds. Infrared spectra (128 scans, 1 cm^{-1}) of the Ti-BEA samples were then taken at 573 K (Fig. S6†). Background spectra were obtained with the empty transmission cell at identical conditions. The vibrational modes on the dehydrated Ti-BEA spectra between 3300–3750 cm^{-1} and 1800–2100 cm^{-1} represent $\nu(O–H)$ of $(SiOH)_x$ groups[54,55] and Si–O–Si overtones[56] of the *BEA framework, respectively. The sharp feature at 3740 cm^{-1} represents isolated SiOH groups that do not interact with other SiOH groups.[54,55] The broader features from 3300 to 3700 cm^{-1} represent defects containing multiple interacting hydroxyl moieties present within $(SiOH)_x$ groups. The ratio of the areas for $\nu(O–H)$ and $\nu(Si–O–Si)$ at 1865 and 2000 cm^{-1} gives a relative measure of SiOH density in each Ti-BEA (Φ_{IR}, eqn (1)). The area of the isolated SiOH feature is excluded from $\nu(O–H)$ in Φ_{IR} calculations. The $\nu(O–H)$ region was deconvoluted into multiple peaks (see Section S1.5†), and the isolated SiOH peak area was subtracted from the combined area of the $\nu(O–H)$ region.

$$\Phi_{IR} = \frac{A_{\nu(O–H)}}{A_{\nu(Si–O–Si)}} \tag{1}$$

The Φ_{IR} values (Table 1) suggest that Ti-BEA-OH contains a density of $(SiOH)_x$ groups nearly one order of magnitude greater than Ti-BEA-F.

Collectively, the characterization results provide strong evidence that Ti-BEA-OH and Ti-BEA-F materials contain atomically dispersed Ti atoms at framework positions within a crystalline *BEA framework. Moreover, these materials lack spectroscopically detectable quantities of TiO_2 nanoparticles or crystallites. Each zeolite contains ~1 Ti atom per 4 unit cells of *BEA, and Ti-BEA-OH contains 2.75 $(SiOH)_x$ nests per unit cell (calculation in ESI Section S1.6†). The synthesis method of Ti-BEA-F prohibits a direct calculation of $(SiOH)_x$ per unit cell, but previously established trends between Φ_{IR} and $(SiOH)_x$[28] indicate that the Ti-BEA-F sample synthesized for this work (Φ_{IR} = 0.27, Table 1) contains < 0.1 $(SiOH)_x$ per unit cell.

2.3 Epoxidation turnover rate measurements

Turnover rates for 1-hexene (C_6H_{12}, Sigma-Aldrich, >99%) epoxidation with hydrogen peroxide (H_2O_2, Fisher Chemical,

30 mol% in H_2O) in aqueous solutions of either acetonitrile (CH_3CN, Fisher Chemical, HPLC Grade), methanol (CH_3OH, Sigma-Aldrich, HPLC, ≥99.9%), or γ-butyrolactone (GBL, $C_4H_6O_2$, Sigma-Aldrich, ≥99%) were measured in three-necked round-bottom flasks with magnetic stirring (700 rpm). The flasks were gently clamped to reflux condensers to avoid evaporative losses and submerged in a temperature-controlled H_2O (308–318 K) or oil (323–338 K) bath on a hot plate (Corning, PC-420D). The reagents (C_6H_{12} and H_2O_2) were combined with H_2O (18.2 MΩ cm, Elga Purelab Flex 2) and CH_3CN, CH_3OH, or $C_4H_6O_2$ along with benzene as an internal standard (Sigma-Aldrich, thiophene-free, >99%) and stirred for 0.5 h before an initial aliquot (~0.5 cm^3) was taken to determine the initial concentration of C_6H_{12} and product, 1,2-epoxyhexane ($C_6H_{12}O$). Ti-BEA (~20–50 mg) was then added to initiate the reaction, and aliquots were taken as a function of time using a syringe equipped with a polypropylene filter (Tisch Scientific, 0.22 μm) to separate the sample from the catalyst particles. The concentrations of alkene, benzene standard, and epoxide product were quantified with a gas chromatograph (Agilent, 6850) equipped with a polysiloxane column (HP-1, Agilent, 19091Z-115E), flame ionization detector, and liquid autosampler (CTC Analytics, GC Pal). Initial turnover rates were determined by fitting turnover numbers (moles of $C_6H_{12}O$ per moles of Ti) as a function of time to a second-order polynomial with the y-intercept fixed at zero and determining the derivative at time equal to zero. All reported turnover rates were measured at differential conversion (<5%), with an uncertainty of ~10% in reported rates, as shown with replicated measurements. The conditions used for rate measurements in this study avoid internal mass transfer constraints, as indicated by the linear dependence of turnover rates on alkene concentration (Section 3.1),[57] which is consistent with expectations based on prior studies of reactions of H_2O_2 with alkenes in Ti substituted MFI, *BEA, and FAU at similar conditions.[29,33,58] A mass-transfer limited material would show a sub-linear dependence on alkene concentration because the mean concentration of alkenes throughout the pores would not depend linearly on the fluid phase alkene concentration.

H_2O_2 consumption rates ($-r_{H2O2}$) were measured with C_6H_{12} present to calculate the selectivities for H_2O_2 consumption (S_{H2O2}) as a co-reactant for epoxidation, as opposed to decomposition between two H_2O_2 molecules to form H_2O and oxygen ($-r_{decomp}$). We note that solvent molecules may react with H_2O_2 to provide another contribution to $-r_{decomp}$, but rate changes with $[H_2O_2]$ suggest that the bimolecular decomposition of H_2O_2 dominates contributions to $-r_{decomp}$ (Fig. 2c). We define H_2O_2 selectivity as the ratio of the epoxidation rate (r_{epox}) to the overall H_2O_2 consumption rate ($-r_{H2O2}$):

$$S_{H_2O_2}(\%) = \frac{r_{epox}}{-r_{H_2O_2}} \times 100 \tag{2}$$

Activation barriers for H_2O_2 decomposition were measured in the absence of C_6H_{12}. Solutions to measure H_2O_2 concentration were prepared using colorimetric titration with a titrant solution consisting of cupric sulfate (8.3 mM; VWR, 99%) and neocuproine hydrate (12 mM; SAGECHEM) in an aqueous

solution of ethanol (4.3 M; Sigma-Aldrich, ≥99.5%). Aliquots from the reactions (0.15 cm^3) were mixed with the titrant (1 cm^3) and DI H$_2$O (0.85 cm^3). The absorbance of this solution at 454 nm was then measured using a UV-Vis spectrophotometer (Spectronic, 20 Genesys) to obtain the H$_2$O$_2$ concentration. A calibration curve was developed with solutions of known H$_2$O$_2$ concentration to convert absorbance to concentration. The concentrations were used to calculate H$_2$O$_2$ decomposition rates by subtracting the formation rate of 1,2-epoxyhexane from the total rate of H$_2$O$_2$ consumption.

2.4 *In situ* analysis of H$_2$O$_2$ activation

H$_2$O$_2$ activation over the Ti-BEA catalysts was examined using a UV-Vis spectrometer (Avantes, AvaSpec-2048) equipped with a pulsed xenon light source (Avantes, AvaLight-XE-Mini). Ti-BEA pellets (7 mm diameter) were loaded into a custom-built liquid flow cell attached to cartridge heaters and a temperature controller (Watlow, EZ-ZONE PM) to hold the cell at 313 K. The cell and spectrometer were connected to a 45-degree fiber optic diffuse reflection probe (Avantes, FC-UVIR600-2-BX-SR). Solvents and H$_2$O$_2$ were introduced continuously to the cell (1 cm^3 min^{-1}) using a high-performance liquid chromatography pump (Teledyne ISCO, ReaXus M1 Class). Background spectra were collected by flowing solvent without H$_2$O$_2$ (10–40 ms integration time, averaging 125–500 scans). Then solvent and H$_2$O$_2$ (0.1 M H$_2$O$_2$, 0.39 M H$_2$O) flowed through the cell until spectra stopped changing (∼0.5 h), which indicated the coverage of H$_2$O$_2$-derived intermediates reached a steady state value. Finally, the cell was purged with flowing solvent without H$_2$O$_2$ for 1 h to examine the reversibility of H$_2$O$_2$ activation.

2.5 Liquid phase adsorption enthalpies for 1,2-epoxyhexane

The heat released upon adsorption of C$_6$H$_{12}$O (TCI Chemicals, >96%) was measured with an isothermal titration calorimeter (ITC) (TA Instruments, NanoITC) equipped with sample and reference cells. A multi-step cleaning procedure was performed to prepare the sample and reference cells for each experiment. A cleaning solution (75 vol% of 1 M NaOH, 20 volume% CH$_3$OH, 5 volume% dish soap) was first injected into the sample cell and left for 5 minutes at room temperature. The sample cell was then rinsed with 500 cm^3 of DI H2O (18.2 MΩ cm, Elga Purelab Flex 2). Next, a 4 M NaOH (VWR, 10 N) solution was left in the cell for 2 hours at 353 K, followed by another rinse with 500 cm^3 of DI H$_2$O. Finally, the cell was treated with a solution of 4 M HNO$_3$ (Macron Chemicals, 68–70 wt%) for 2 hours at 353 K, then a third rinse with 500 cm^3 of DI H$_2$O. The sample cell, reference cell, and 50 μL ITC syringe were then filled with H$_2$O, and the syringe was loaded into the instrument. A subsequent electrical calibration used sequential pulses to determine the heat released from a calibrated Pt resistor. Finally, pure DI H$_2$O was injected into DI H$_2$O to ensure that the sample cell was clean enough to begin experiments. The cell was assumed to be clean when the H$_2$O–H$_2$O injection released negligible amounts of heat (±3 μJ for each injection of 1 μL). The cleaning procedure was repeated if the H$_2$O–H$_2$O injection did not give sufficiently low heat rates.

In a typical experiment, a slurry of Ti-BEA (15–30 mg) in organic solvent with H$_2$O was titrated by a solution of epoxide (5–10 mM C$_6$H$_{12}$O) in the same solvent mixture. The mass of Ti-BEA in the sample cell was calculated by taking the difference between the mass added to the slurry and the mass remaining upon evaporation of the residual slurry after loading the cell. H$_2$O concentrations were chosen to match conditions for kinetic turnover rate measurements (Section 3.1). The titrations were carried out at 313 K with a stirring rate of 250 rpm. The enthalpies of epoxide adsorption were calculated by averaging the integrated heats released upon adsorption of the epoxides to Ti-BEA sites from a 1 μL injection of titrant at low coverages (<0.25 mol epoxide (mol Ti)$^{-1}$). The heats released in this low coverage regime remain approximately constant, suggesting that the calculated enthalpies represent the isosteric adsorption enthalpies for each epoxide.[28]

2.6 Liquid phase absorption of aqueous solvents

A nuclear magnetic resonance (NMR) spectrometer (Unity, INOVA 500 NB) was used to calculate the equilibrium compositions of aqueous solutions of organic solvents contacted to and equilibrated with Ti-BEA-OH and Ti-BEA-F samples by measuring ^{1}H NMR peak areas. For each data point, an aliquot (∼0.25 cm^3) of organic solvent and H$_2$O was taken from a solvent solution (5 cm^3) before and after 2 h contact with a Ti-BEA sample (∼500 mg) at a stirring rate of 700 rpm and temperature of 313 K to measure the change in the bulk liquid phase concentration. The catalyst and solvent mixture were in contact for 2 h to ensure solvent absorption had reached equilibrium. The sample of organic solvent and H$_2$O was then mixed with deuterated methanol (CD$_3$OD) as solvent and acetone or chloroform as an internal standard to prepare the NMR sample. The initial and final composition of the extrapore liquid was determined using areas of ^{1}H-NMR features for H$_2$O (4.5 ppm), acetone (2.2 ppm) or chloroform (7.8 ppm), and the organic solvent (CH$_3$CN at 2.1 ppm, CH$_3$OH at 3.3 ppm, C$_4$H$_6$O$_2$ features at 2.3, 2.6 and 4.5 ppm). The intrapore solvent composition was estimated from the amount of solvent absorbed by the catalyst and the difference in extrapore liquid phase concentration before and after contacting the solvent with the catalyst (ESI Section S2†).

3. Results and discussion

3.1 Epoxidation and H$_2$O$_2$ decomposition rates depend on aqueous solvent composition

Fig. 1 shows that turnover rates for C$_6$H$_{12}$ epoxidation and H$_2$O$_2$ decomposition depend strongly on the identity of the organic component of the aqueous solvent and the value of x_{H_2O}. Turnover rates span four-orders of magnitude and, consequently, lead to H$_2$O$_2$ selectivities ($S_{H_2O_2}$) that range from 0.1–98%. Fig. 1a shows that rates of C$_6$H$_{12}$ epoxidation increase as x_{H_2O} increases for all organic solvents over both Ti-BEA-OH and Ti-BEA-F. Ti-BEA-OH gives greater rates than Ti-BEA-F for each organic solvent at all x_{H_2O}. This systematic difference was previously attributed to entropy gains that reflect the disruption
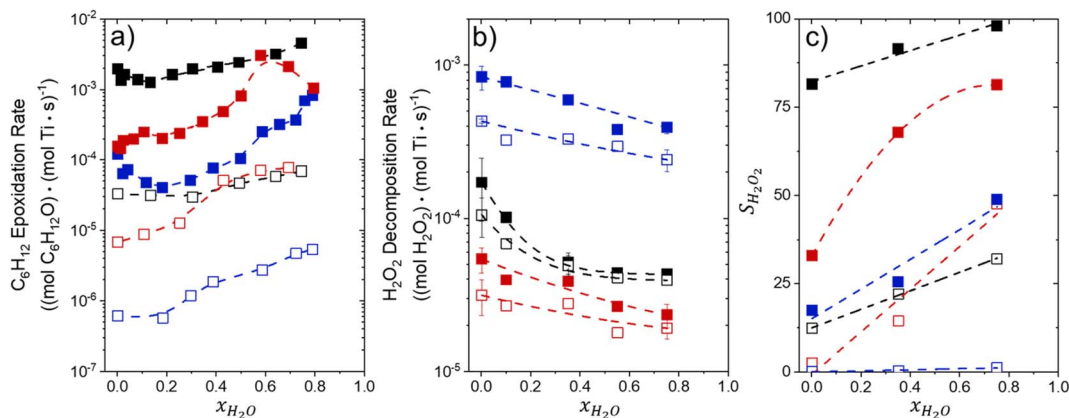
Fig. 1 Turnover rates for (a) C_6H_{12} epoxidation to form $C_6H_{12}O$ (1 mM C_6H_{12}, 10 mM H_2O_2, 313 K), (b) H_2O_2 decomposition (1 mM H_2O_2, 313 K), and (c) H_2O_2 selectivities for epoxidation (1 mM C_6H_{12}, 10 mM H_2O_2, 313 K) as a function of H_2O mole fraction in mixtures of CH_3CN (■,□), CH_3OH (■,□), and $C_4H_6O_2$ (■,□) with H_2O over Ti-BEA-OH (solid points) and Ti-BEA-F (hollow points). The furthest left data points represent $x_{H_2O} = 0.002$, which comes from the aqueous H_2O_2 reagent solution (39 mM).

of greater quantities of hydrogen bonded H_2O molecules in hydrophilic pores of Ti-BEA.[27,33,34] Epoxidation turnover rates in $C_4H_6O_2$ are consistently lowest among these organic solvents at all x_{H_2O}. CH_3CN provides the greatest rates in all cases except when x_{H_2O} exceeds 0.4 over Ti-BEA-F, where rates in CH_3OH surpass those in CH_3CN.

Fig. 1b shows that turnover rates for H_2O_2 decomposition (*i.e.*, in the absence of C_6H_{12}) decrease with increasing x_{H_2O} for all combinations of organic solvent and zeolite, which opposes the trend for epoxidation turnover rates. Among organic solvents, $C_4H_6O_2$ gives the greatest H_2O_2 decomposition rates and CH_3OH gives the lowest rates at all x_{H_2O}. The lower H_2O_2 decomposition rates in CH_3OH than in CH_3CN mixtures agree with previous reports over Ti-incorporated zeolite materials,[39,44] while turnover rates for C_6H_{12} epoxidation in CH_3CN that are greater than those in CH_3OH mixtures concur with findings over Ti-BEA materials.[29,37–39] Notably, H_2O_2 decomposition rates in Fig. 1b span less than two-orders of magnitude, which shows the decomposition pathway senses the identity of the solvent and zeolite less strongly than C_6H_{12} epoxidation. The contrasting effects of organic solvent and x_{H_2O} on epoxidation and H_2O_2 decomposition rates evince that solvent molecules influence the stability of the fluid phase reactants and transition states within pores for the two pathways in different ways.

Fig. 1c reveals that all combinations of organic solvents and zeolites show significantly higher $S_{H_2O_2}$ for C_6H_{12} epoxidation at greater x_{H_2O}. Ti-BEA-OH gives greater values of $S_{H_2O_2}$ than Ti-BEA-F in all cases, but $S_{H_2O_2}$ increases more with x_{H_2O} over Ti-BEA-F relative to Ti-BEA-OH (see ESI Section S3†). The greatest $S_{H_2O_2}$ (98%) occurs in Ti-BEA-OH with aqueous CH_3CN (x_{H_2O} = 0.75) (Note: values of x_{H_2O} greater than 0.8 were not used due to miscibility issues with C_6H_{12}). Overall, CH_3CN mixtures lead to the highest $S_{H_2O_2}$ and $C_4H_6O_2$ leads to the lowest $S_{H_2O_2}$ at all x_{H_2O} in Ti-BEA-OH. This trend holds at lower x_{H_2O} values (≤0.35) in Ti-BEA-F, but CH_3OH gives the highest $S_{H_2O_2}$ at higher x_{H_2O} (≥0.75). Collectively, the data presented in Fig. 1 shows that increasing x_{H_2O} within each organic solvent provides greater

epoxidation rates and more selective use of H_2O_2 for epoxidation over Ti-BEA zeolites with different $(SiOH)_x$ densities.

The differences in turnover rates for C_6H_{12} epoxidation (Fig. 1a) and H_2O_2 decomposition (Fig. 1b) may result from changes in the coverage of reactive species, the reaction mechanism, or the kinetically relevant step; alternatively, these differences may reflect changes in the free energies of reagents, reactive intermediates, or key transition states due to direct interactions with solvent molecules. The coming sections distinguish these possibilities using the molecular interpretation of turnover rate expressions for the epoxidation and H_2O_2 decomposition reactions.

3.2 x_{H_2O} does not influence reaction mechanisms

Turnover rates for epoxidation and H_2O_2 decomposition reflect the stabilities of the associated transition states together with the coverages of reactive surface species formed during catalysis, which depend on the concentrations of the reactants and products present. Fig. 2a shows that C_6H_{12} epoxidation rates depend linearly on C_6H_{12} concentration ([C_6H_{12}], where brackets denote the concentration of a species or the number of surface intermediates) at low ratios of [C_6H_{12}] to [H_2O_2] (<0.5) in aqueous CH_3OH mixtures over both Ti-BEA-OH and Ti-BEA-F. At these low ratios of [C_6H_{12}] to [H_2O_2], rates do not depend on values of [H_2O_2] (Fig. 2b). Rates show a sublinear dependence on [C_6H_{12}] at higher ratios of [C_6H_{12}] to [H_2O_2], which signifies a change in the most abundant reactive intermediate (MARI). In contrast, turnover rates for epoxidation depend weakly on [C_6H_{12}], linearly on [H_2O_2], and inversely on epoxide product concentration ([$C_6H_{12}O$]) at sufficiently high ratios of [C_6H_{12}] to [H_2O_2] ([C_6H_{12}]:[H_2O_2] > 50), consistent with previous work.[58,59] Fig. 2c demonstrates, however, that H_2O_2 decomposition turnover rates increase linearly with [H_2O_2] on both Ti-BEA materials for all x_{H_2O} examined. Measurements obtained from aqueous solutions of CH_3CN and $C_4H_6O_2$ (ESI Section S4†) exhibit effects of reactant concentrations on epoxidation and H_2O_2 decomposition turnover rates that match
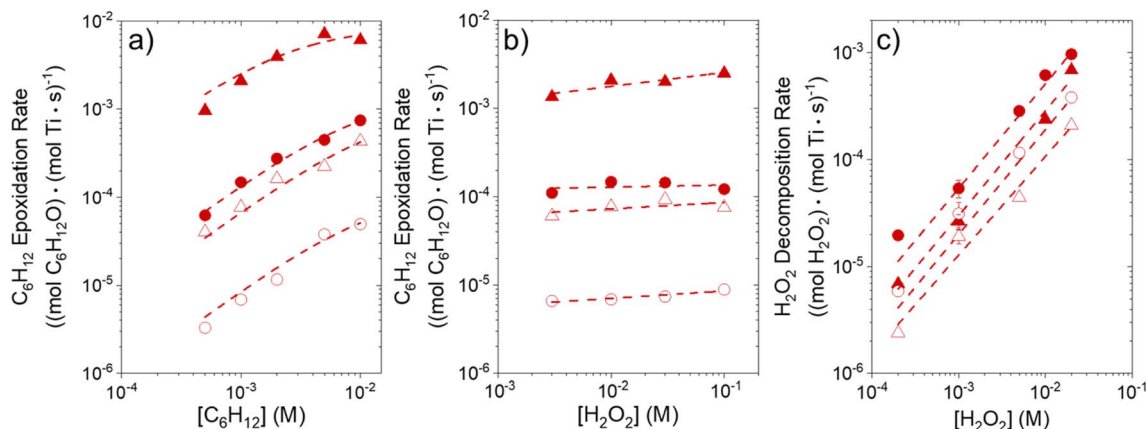
Fig. 2 Turnover rates for C_6H_{12} epoxidation as a function of (a) C_6H_{12} concentration (10 mM H_2O_2, 313 K), and (b) H_2O_2 concentration (1 mM C_6H_{12}, 313 K), and turnover rates for (c) H_2O_2 decomposition (313 K) as a function of H_2O_2 concentration for CH_3OH mixtures with the minimum or maximum water contents examined (39 mM H_2O, x_{H_2O} = 0.002 (●,○); ~31.6 M H_2O, x_{H_2O} = 0.75 (▲,△)) over Ti-BEA-OH (solid points) and Ti-BEA-F (hollow points).

the behavior in aqueous CH_3OH (Fig. 2). Collectively, these observations match the manner in which turnover rates for epoxidation of 1-alkenes (C_6H_{12} to $C_{18}H_{36}$),[27,29,33,34,58,60,61] cyclohexene,[59] and styrene[62–64] with H_2O_2 depend upon concentrations of reactants and products in CH_3CN[27,29,33,58–64] and CH_3OH[29,64] upon a range of titanosilicates (Ti-MFI,[29,33] Ti-BEA,[27,29,58,59,61–63] Ti-FAU[33,63] Ti–SiO$_2$[60–63]) and Fe- and Cr-incorporated metal–organic frameworks,[64] which implies that conclusions for the effects of x_{H_2O} on epoxidation kinetics for C_6H_{12} should extend broadly across alkenes.

Scheme 2 depicts a plausible system of elementary steps that describe the epoxidation of C_6H_{12} and the bimolecular decomposition of H_2O_2. The catalytic cycle begins with quasi-equilibrated adsorption of a solvent molecule (step 0), C_6H_{12} (step 1), or H_2O_2 (step 2). Then, H_2O_2 activates to form a pool of Ti–OOH[58,65–70] and titanium-peroxo (Ti-$(\eta^2$-O$_2$))[58,62,69,70] intermediates (step 3). The H_2O_2-derived intermediates may protonate to reform H_2O_2 (reverse of step 3), react with C_6H_{12} to form $C_6H_{12}O$ (step 4), or react with a fluid phase H_2O_2 molecule to decompose to water and oxygen (step 6) in kinetically relevant processes. Radical clock experiments performed with *cis*-stilbene[58] give evidence that Ti–OOH intermediates, commonly

product (step 5) and complete the catalytic cycle. This scheme accounts for differences in the apparent dependence of rates on reactant concentrations at low and high ratios of $[C_6H_{12}]$ to $[H_2O_2]$. While O-atom transfer from Ti–OOH to C_6H_{12} remains the kinetically relevant step for each kinetic regime,[58] the MARI differs between the regimes. Ti–OOH intermediates saturate active sites at low ratios of $[C_6H_{12}]$ to $[H_2O_2]$, and the $C_6H_{12}O$ product covers these sites at high ratios of $[C_6H_{12}]$ to $[H_2O_2]$. Based upon Scheme 2 and the kinetic relevance of each step depicted, epoxidation rates (r_{epox}) follow a simple rate expression:

$$r_{epox} = k_4[\text{Ti–OOH}][C_6H_{12}] \quad (3)$$

where k_4 is the rate constant for step 4 (Scheme 2) and [Ti–OOH] represents the number of the H_2O_2-derived surface intermediates. Applying the pseudo-steady state hypothesis to Ti–OOH intermediates and a site balance yields a turnover rate expression (see Section S6† for full derivation) consistent with rate measurements:

$$\frac{r_{epox}}{[L]} = \frac{\dfrac{k_3 k_4 K_2[C_6H_{12}][H_2O_2]}{k_{-3} + k_4[C_6H_{12}] + k_6[H_2O_2]}}{K_0[S] + K_1[C_6H_{12}] + K_2[H_2O_2] + \dfrac{k_3 K_2[H_2O_2]}{k_{-3} + k_4[C_6H_{12}] + k_6[H_2O_2]} + \dfrac{[C_6H_{12}O]}{K_5}} \quad (4)$$

invoked as the reactive intermediate for epoxidations,[58,62,69,71,72] primarily participate in the transfer of O-atoms to alkenes to form epoxides (rather than Ti-$(\eta^2$-O$_2$)). We, therefore, refer to the pool of H_2O_2-derived intermediates as Ti–OOH for simplicity. The formed epoxide then desorbs in a quasi-equilibrated manner to release the 1,2-epoxyhexane ($C_6H_{12}O$)

Fig. 3 presents evidence that the values of k_{-3} depend on the identity of the organic solvent and x_{H_2O}. *In situ* UV-Vis spectra give strong evidence that the H_2O_2-derived intermediates form reversibly in H_2O (Fig. 3a) and irreversibly in $C_4H_6O_2$ (Fig. 3b). Notably, the peak areas for Ti–OOH and Ti–(η^2)–O$_2$ attenuate by ~60% in H_2O (Fig. 3a) and by ~6% in $C_4H_6O_2$ (Fig. 3b) over a 1 h
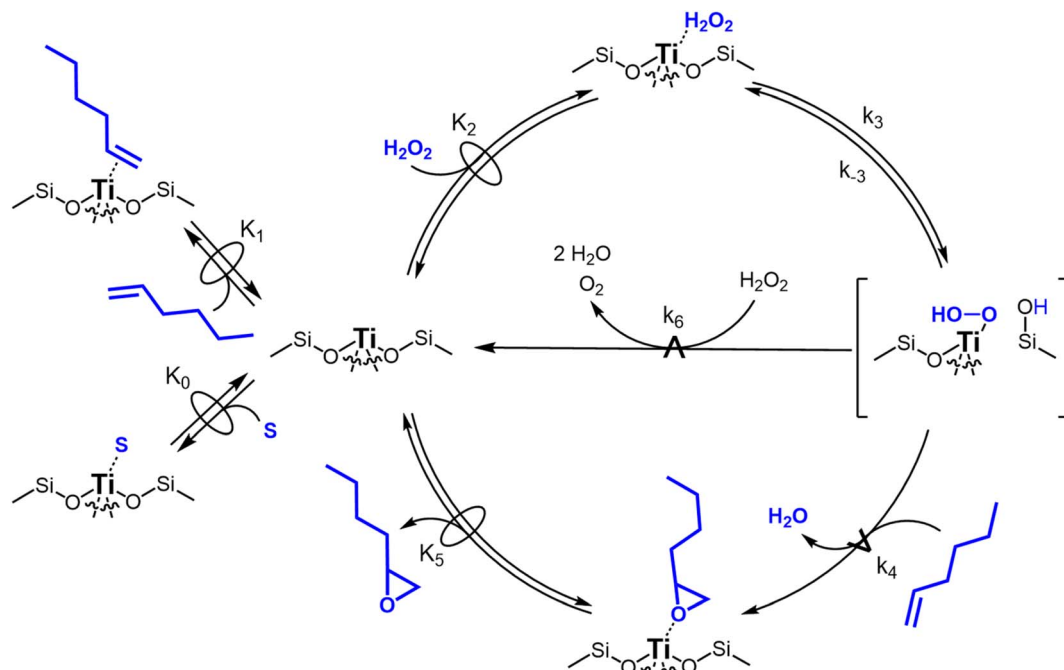
Scheme 2 Proposed mechanism for C_6H_{12} epoxidation with H_2O_2 and H_2O_2 decomposition on Ti-BEA catalysts. ⇌ denotes a quasi-equilibrated step, while —A→ signifies kinetically relevant steps for formation of distinct products. The degree of reversibility of H_2O_2 activation (step 3) varies with the quantity of protic molecules in the solvent. The blue H atom in the Si—OH group adjacent to Ti—OOH originates from H_2O_2 during Ti—OOH formation. Solvent molecules have been omitted for clarity, except for the adsorption of a solvent molecule (S) to Ti sites in step 0.

Fig. 3 *In situ* UV-Vis spectra of Ti-BEA-OH as a function of time within continuously flowing neat (a) H_2O, (b) $C_4H_6O_2$, and (c) equimolar H_2O and $C_4H_6O_2$ (313 K, 1 cm^3 min^{-1}) after H_2O_2 activation (100 mM H_2O_2, 390 mM H_2O, 313 K, 1 cm^3 min^{-1}). Spectra were acquired every 600 s after H_2O_2 activation. Spectra for Ti-BEA-F and desorption rate constants are included in Section S5.†

period after switching from an aqueous H_2O_2 solution to the neat solvent. Prior UV-Vis spectra suggest irreversible H_2O_2 activation in CH_3CN[29,59,62] and reversible activation in CH_3OH.[29,69] Therefore, these findings lead to the broader conclusion that protic solvents (*i.e.*, H_2O, CH_3OH) protonate Ti–OOH and Ti–(η^2–O_2), which then desorb as H_2O_2, but these

steps are much slower in aprotic solvents (*i.e.*, CH_3CN, $C_4H_6O_2$). The H_2O_2 intermediate peak areas also attenuate by ∼40% in 1 h in an equimolar mixture of H_2O and $C_4H_6O_2$ (Fig. 3c), which indicates that including a sufficient quantity of a protic component within a solvent mixture allows for reversible H_2O_2 activation. These findings demonstrate that H_2O_2 may reform

from Ti–OOH and Ti–(η^2-O_2) within all aqueous solvent combinations utilized here, where the rate of reformation depends on the concentration of protic solvent molecules present. Values of k_{-3} over Ti-BEA zeolites in CH_3OH are up to 10-times greater than in neat H_2O (Table S3†),[29] which suggests that CH_3OH facilitates the reformation of H_2O_2 more readily than H_2O.

Despite the variations in the reversibility of H_2O_2 activation across solvent mixtures, the full rate expression (eqn (4)) simplifies to a common form when Ti–OOH intermediates saturate active sites (*i.e.*, [Ti–OOH] $\approx$ [L]).

$$\frac{r_{\text{epox}}}{[L]} = k_4[C_6H_{12}] \qquad (5)$$

Eqn (5) predicts rates that match the data in Fig. 2a (at $[C_6H_{12}]:[H_2O_2] < 0.5$) and 2b, implicating Ti–OOH intermediates as the MARI for epoxidation. Notably, Fig. S9† and 2 together demonstrate that the regime of a Ti–OOH MARI and first-order kinetics with respect to $[C_6H_{12}]$ holds for each combination of catalyst, organic solvent, and x_{H_2O} when molar ratios of H_2O_2 to C_6H_{12} exceed two.

Rates for H_2O_2 decomposition depend on the coverage of Ti–OOH and $[H_2O_2]$ because H_2O_2 decomposition involves a reaction between a Ti–OOH intermediate and a fluid phase H_2O_2 molecule. Therefore, H_2O_2 decomposition rates correspond to:

$$-r_{\text{decomp}} = k_6[\text{Ti–OOH}][H_2O_2] \qquad (6)$$

where k_6 is the rate constant for step 6 in Scheme 2. Substituting terms for [Ti–OOH] and using the site balance for [L] gives a full rate expression:

$$\frac{-r_{\text{decomp}}}{[L]} = \frac{\dfrac{k_3 k_4 K_2 [H_2O_2]^2}{k_{-3} + k_4[C_6H_{12}] + k_6[H_2O_2]}}{K_S[S] + K_1[C_6H_{12}] + K_2[H_2O_2] + \dfrac{k_3 K_2[H_2O_2]}{k_{-3} + k_4[C_6H_{12}] + k_6[H_2O_2]} + \dfrac{[C_6H_{12}O]}{K_5}} \qquad (7)$$

Once again, the rate expression simplifies when Ti–OOH intermediates saturate active sites, such that eqn (7) collapses to the form:

$$\frac{-r_{\text{decomp}}}{[L]} = k_6[H_2O_2] \qquad (8)$$

The rate expression in eqn (8) reproduces the turnover rate dependencies on $[H_2O_2]$ shown in Fig. 2c. This interpretation also agrees with prior studies that invoked a mechanism in which fluid phase H_2O_2 reacts with an H_2O_2-derived intermediate over Ti-,[65,73] Nb-,[74] and Ta-incorporated[75] microporous and mesoporous catalysts.

Notably, applying Ti–OOH as the MARI yields equations that match the data for C_6H_{12} epoxidation (eqn (5)) and H_2O_2 decomposition (eqn (8)) in Fig. 2 simultaneously. The two

pathways, therefore, proceed through the common reaction intermediate (Ti–OOH) that remains the MARI at all x_{H_2O} examined here in each zeolite. As shown for epoxidation rates, the simplified decomposition rate expression (eqn (8)) does not reflect the value of k_{-3}, which implies that the reversibility of H_2O_2 activation does not impact rates of alkene epoxidation and H_2O_2 decomposition within the regime where Ti–OOH intermediates saturate active sites. This analysis indicates that kinetic measurements made under these conditions provide the requisite platform for direct and quantitative comparisons between solvent – catalyst pairs.

To summarize, similar rate dependences for both Ti-BEA-OH and Ti-BEA-F at high (0.002) and low (0.75) x_{H_2O} in each organic solvent suggest that epoxidation and H_2O_2 decomposition proceed through the same reaction mechanisms. Differences in epoxidation rates with different organic solvents, concentrations of water, and $(SiOH)_x$ defect densities within pores of *BEA (Fig. 1) do not result from changes in the reaction mechanisms or coverage of reactive species. These findings resemble the interpretation of prior investigations for homogeneous acid-catalyzed alcohol dehydration reactions that concluded solvent molecules influence the stability of fluid phase reactive species.[10,76–78] Our group and others showed that solvent molecules within zeolite pores affect the stability of adsorbed reactive species for alkene epoxidation with H_2O_2,[27,29,33] glucose isomerization,[48,79–81] and alcohol dehydration.[82–86] With mechanistic differences excluded, the rate differences for epoxidation and H_2O_2 decomposition in Fig. 1 and 2 must reflect interactions among solvent molecules and reactive species located both within pores and within the bulk solvent that drive changes in k_4 (eqn (5)) and k_6 (eqn (8)).

3.3 Activity coefficients show differences in intrapore and fluid phase species stability

Activity coefficients (γ) of the fluid phase reactants (C_6H_{12} and H_2O_2; $\gamma_{C_6H_{12}}$ and $\gamma_{H_2O_2}$) contribute to observed differences between turnover rates. Prior studies correlated values of fluid phase γ for 5-hydroxymethylfurfural[87] and glucose[48] to etherification and isomerization rates, respectively. Here, thermodynamic models were used to directly quantify γ values to determine how reagent stability changes with x_{H_2O} and organic solvent identity (ESI Section S7†). Fig. 4 shows turnover rates for C_6H_{12} epoxidation and H_2O_2 decomposition normalized by γ values of the respective reactant at each x_{H_2O}, which accounts for the influence of intramolecular interactions (*i.e.*, excess contributions) on the stability of the reactant in the fluid phase. When normalized by solvent-dependent values of $\gamma_{C_6H_{12}}$, the

Fig. 4 Turnover rates for (a) $C_6H_{12}O$ formation (1 mM C_6H_{12}, 10 mM H_2O_2, 313 K) normalized by $\gamma_{C_6H_{12}}$ and (b) H_2O_2 decomposition (1 mM H_2O_2, 313 K) normalized by $\gamma_{H_2O_2}$ as a function of x_{H_2O} in mixtures of CH_3CN (■, □), CH_3OH (■, □), and $C_4H_6O_2$ (■, □) with H_2O over Ti-BEA-OH (solid points) and Ti-BEA-F (hollow points). Activity coefficients of C_6H_{12} were calculated using the Volume-Translated Peng-Robinson (VTPR) method on ChemCAD, while activity coefficients of H_2O_2 were calculated with the nonrandom two-liquid (NRTL) method.

epoxidation turnover rates still span three-orders of magnitude and depend on both x_{H_2O} and the identity of the organic component of the solvent (Fig. 4a). In addition, the changes in activity-normalized turnover rates $\left(\dfrac{r_{epox}}{[L] \times \gamma_{C_6H_{12}}}\right)$ as functions of x_{H_2O} exhibit complex non-monotonic dependences, which may reflect the influence of pore confinement on the solvation shells of reactive species and transition states within *BEA pores. Indeed, these data indicate that the stabilities of reactive species in the pore (G_{Ti-OOH}, $G^{\ddagger}_{epox}$) change with x_{H_2O} and affect rates significantly. Accounting for $\gamma_{C_6H_{12}}$ and $\gamma_{H_2O_2}$ values within turnover rate expressions for C_6H_{12} epoxidation and H_2O_2 decomposition when Ti–OOH covers sites (eqn (5) and (8)) and defining alternate rate constants (k_4^* and k_6^*) yields:

$$\frac{r_{epox}}{[L] \times \gamma_{C_6H_{12}}} = k_4^*[C_6H_{12}] \tag{9}$$

$$\frac{-r_{decomp}}{[L] \times \gamma_{H_2O_2}} = k_6^*[H_2O_2] \tag{10}$$

where k_4^* and k_6^* depend on corresponding alternate apparent activation free energies ($\Delta G^{*\ddagger}_{app}$) (see Section 3.4†). The non-monotonic trends in Fig. 4a must stem from differences in the structure and composition of the solvation shells for Ti-bound intermediates and transition states as a function of organic solvent, x_{H_2O}, and zeolite $(SiOH)_x$ density. The Ti–OOH intermediate and epoxidation transition state likely have different sizes and polarities (Scheme 3a), which promote different stoichiometries of water and co-solvent within their solvation shells.
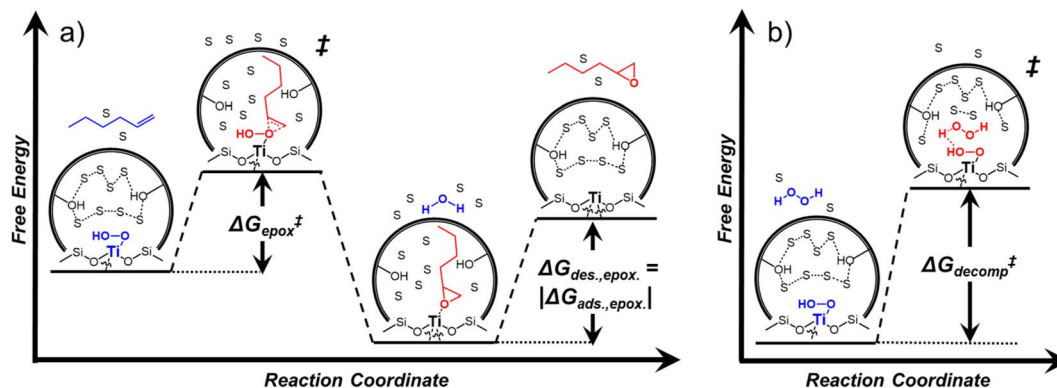
Scheme 3 Proposed reaction coordinate diagrams for (a) C_6H_{12} epoxidation and (b) H_2O_2 decomposition over Ti-BEA zeolites, where solvent molecules are organic solvent or H_2O and are denoted with an "S". In (a), the alkene adsorbs into the pore and reacts with the Ti–OOH MARI to form the epoxide. The epoxide then desorbs to complete the reaction. In (b), the liquid phase H_2O_2 adsorbs and binds to the Ti–OOH MARI to form the transition state. The remainder of the reaction coordinate in which the products form ($2H_2O + O_2$) is not shown for brevity.

Fig. 4b reveals that rates for H_2O_2 decomposition normalized by $\gamma_{H_2O_2}$ $\left(\frac{-r_{\text{decomp}}}{[L] \times \gamma_{H_2O_2}}\right)$ increase systematically with increasing x_{H_2O} in all combinations of zeolite and organic solvent. The decomposition transition state and Ti–OOH plausibly form hydrogen bonds with multiple H_2O molecules (Scheme 3b), which stabilize these species at higher x_{H_2O}. Transition state stabilization through hydrogen bonds with H_2O may outweigh the same effect for Ti–OOH because the transition state contains more hydrogen bonding functions. This disparity in hydrogen bond donating and accepting interactions generates the trends in activity-normalized turnover rates in Fig. 4b (eqn (10)). Overall, $\frac{-r_{\text{decomp}}}{[L] \times \gamma_{H_2O_2}}$ values change less significantly with x_{H_2O} than $\frac{r_{\text{epox}}}{[L] \times \gamma_{C_6H_{12}}}$, indicating that differences in Ti–OOH stability largely cancel out with the decomposition transition state but differ more significantly from epoxidation transition state stability. The differences between the sensitivities of these reaction pathways to x_{H_2O} reflect the distinct size and structure of solvation shells surrounding the corresponding transition states within the pores of Ti-BEA catalysts and indicate that solvent molecules assist with the selective stabilization of certain transition states for these parallel pathways.

Variations between the trends for turnover rates in Fig. 1 and for $\frac{r_i}{[L] \times \gamma_i}$ values in Fig. 4 and their dependence on x_{H_2O} directly reflect the stabilization of fluid phase C_6H_{12} and H_2O_2 by interactions with fluid phase solvent molecules. As x_{H_2O} increases ($0.002 \leq x_{H_2O} \leq 0.8$), $\gamma_{C_6H_{12}}$ increases by factors of 12–15 while $\gamma_{H_2O_2}$ decreases by 3–6 fold (Fig. S13 and S14†). These opposing changes result from destabilizing interactions between hydrophobic C_6H_{12} and H_2O and stabilizing interactions between hydrophilic H_2O_2 and H_2O. These γ trends correspond to the rate trends for C_6H_{12} epoxidation and H_2O_2 decomposition in Fig. 1. The persistent dependence of $\frac{r_i}{[L] \times \gamma_i}$ values in Fig. 4 on organic solvent identity, x_{H_2O}, and $(SiOH)_x$ density establishes that the stability of transition states and Ti–OOH intermediates in the pore respond to changes in fluid composition within the pores of *BEA. The following section provides further insight and quantitatively assesses the effect of x_{H_2O} on the stability of reactive species in the pores with activation barrier measurements.

3.4 Stability of reactive species vary with organic solvent, x_{H_2O}, and $(SiOH)_x$ density

Turnover rate measurements (Fig. 1 and 2) show that C_6H_{12} epoxidation and H_2O_2 decomposition turnover rates depend on the organic solvent, x_{H_2O}, and $(SiOH)_x$ density of Ti-BEA. The first two factors alter the solvent environment around reactive species in the bulk fluid phase, whereas all three factors influence the solvation of species at active sites within the pores of Ti-BEA. Consequently, these variables impact apparent activation enthalpies ($\Delta H_{\text{app}}^{\ddagger}$) and entropies ($\Delta S_{\text{app}}^{\ddagger}$) for epoxidation ($\Delta H_{\text{app,epox}}^{\ddagger}$, $\Delta S_{\text{app,epox}}^{\ddagger}$) and H_2O_2 decomposition ($\Delta H_{\text{app,decomp}}^{\ddagger}$, $\Delta S_{\text{app,decomp}}^{\ddagger}$). Values of $\Delta H_{app}^{\ddagger}$ and $\Delta S_{\text{app}}^{\ddagger}$ were

measured in identical kinetic regimes, where C_6H_{12} or H_2O_2 react with the Ti–OOH MARI to form the corresponding transition states (Scheme 3). The apparent activation free energy ($\Delta G_{\text{app}}^{\ddagger}$) depends on $\Delta H_{\text{app}}^{\ddagger}$ and $\Delta S_{\text{app}}^{\ddagger}$ and can be defined as the difference between the free energy of the transition state and reference state components, shown here for C_6H_{12} epoxidation:

$$\Delta G_{\text{app,epox}}^{\ddagger} = \left(G_{\text{epox}}^{\ddagger,0} + G_{\text{epox}}^{\ddagger,\varepsilon}\right) - \left(G_{\text{Ti-OOH}}^{0} + G_{\text{Ti-OOH}}^{\varepsilon}\right)$$
$$- \left(G_{C_6H_{12}}^{0} + G_{C_6H_{12}}^{\varepsilon}\right) \qquad (11)$$

where free energies contain both standard state (G^0) and excess (G^ε) contributions. The excess free energy for a species i can be calculated from the activity coefficient for that species (γ_i), which depends on interactions with solvating molecules or nearby surfaces.

$$G_i^{\varepsilon} = RT \times \ln(\gamma_i) \qquad (12)$$

The excess free energies equal zero for ideal solutions (i.e., when the activity coefficient equals one) but are non-zero in non-ideal solutions and at solid–liquid interfaces.[26] We can define apparent free energy terms ($\Delta G_{\text{app}}^{*\ddagger}$) that exclude the activity coefficient of the reactant (i.e., C_6H_{12}), which correspond to the k_4^* term represented in eqn (9):

$$k_4^* = \frac{k_B T}{h} \exp\left(-\frac{\Delta G_{\text{app,epox}}^{*\ddagger}}{RT}\right) \qquad (13)$$

To define $\Delta G_{\text{app}}^{*\ddagger}$ values, we must simply add $G_{C_6H_{12}}^{\varepsilon}$ to each side of eqn (11):

$$\Delta G_{\text{app,epox}}^{*\ddagger} = \Delta G_{\text{app,epox}}^{\ddagger} + G_{C_6H_{12}}^{\varepsilon}$$
$$= \left(G_{\text{epox}}^{\ddagger,0} + G_{\text{epox}}^{\ddagger,\varepsilon}\right) - \left(G_{\text{Ti-OOH}}^{0} + G_{\text{Ti-OOH}}^{\varepsilon}\right) - G_{C_6H_{12}}^{0} \qquad (14)$$

Note, an identical derivation of equations for H_2O_2 decomposition is included in the ESI (Section S6†). Values for $\gamma_{C_6H_{12}}$ were used to compute $H_{C_6H_{12}}^{\varepsilon}$ (Section S7†). The $H_{C6H_{12}}^{\varepsilon}$ values allow for the derivation of an enthalpy term ($\Delta H_{\text{app,epox}}^{*\ddagger}$) analogous to $\Delta G_{\text{app,epox}}^{*\ddagger}$:

$$\Delta H_{\text{app,epox}}^{*\ddagger} = \Delta H_{\text{app,epox}}^{\ddagger} + H_{C_6H_{12}}^{\varepsilon}$$
$$= \left(H_{\text{epox}}^{\ddagger,0} + H_{\text{epox}}^{\ddagger,\varepsilon}\right) - \left(H_{\text{Ti-OOH}}^{0} + H_{\text{Ti-OOH}}^{\varepsilon}\right) - H_{C_6H_{12}}^{0} \qquad (15)$$

Likewise, $\gamma_{H_2O_2}$ values yield values for $H_{H_2O_2}^{\varepsilon}$ (ESI Section S7†), which allows for the calculation of a similar enthalpic term for H_2O_2 decomposition ($\Delta H_{\text{app,decomp}}^{*\ddagger}$):

$$\Delta H_{\text{app,decomp}}^{*\ddagger} = \Delta H_{\text{app,decomp}}^{\ddagger} + H_{H_2O_2}^{\varepsilon}$$
$$= \left(H_{\text{decomp}}^{\ddagger,0} + H_{\text{decomp}}^{\ddagger,\varepsilon}\right) - \left(H_{\text{Ti-OOH}}^{0} + H_{\text{Ti-OOH}}^{\varepsilon}\right)$$
$$- H_{H_2O_2}^{0} \qquad (16)$$

Fig. 5 $\Delta H^{*\ddagger}_{app,epox}$ values for C_6H_{12} epoxidation (1 mM C_6H_{12}, 10 mM H_2O_2, 308–333 K) as a function of x_{H_2O} in mixtures of (a) CH_3OH (■,□), (b) CH_3CN (■,□), and (c) $C_4H_6O_2$ (■,□) with H_2O over Ti-BEA-OH (solid) and Ti-BEA-F (hollow).

ESI Section S9† includes the measured $\Delta H^{\ddagger}_{app}$ and $\Delta S^{\ddagger}_{app}$ for each pathway and discusses the entropy trends, which align with the interpretation of the enthalpy trends that follow. Eqn (15) and (16) account for the dependence of enthalpy values on organic solvent identity, x_{H_2O}, and $(SiOH)_x$ density. The values of $H_{C_6H_{12}}0$ and $H_{H_2O_2}0$ do not depend on these variables, so differences in $\Delta H^{*\ddagger}_{app,epox}$ and $\Delta H^{*\ddagger}_{app,decomp}$ arise entirely from changes in H^ε values for the Ti–OOH intermediate and respective transition states.

Fig. 5 shows that $\Delta H^{*\ddagger}_{app,epox}$ varies as a function of x_{H_2O} between Ti-BEA-OH and Ti-BEA-F, which indicates that the organization, density, and composition of solvent molecules within the pores of *BEA differ between these materials. Across organic solvents, $\Delta H^{*\ddagger}_{app,epox}$ values span 4–19 kJ mol^{-1} between the lowest and highest x_{H_2O} for Ti-BEA-F and 12–32 kJ mol^{-1} over Ti-BEA-OH. These comparisons give evidence that the solvent structure in Ti-BEA-OH pores changes more significantly with increasing x_{H_2O} than in Ti-BEA-F. $\Delta H^{*\ddagger}_{app,epox}$ increases with increasing x_{H_2O} for CH_3OH (Fig. 5a) and CH_3CN

(Fig. 5b) mixtures over Ti-BEA-OH, which may indicate the transition state disrupts a greater quantity of H_2O within pores, which increases $H^{\ddagger,\varepsilon}_{epox}$. For $C_4H_6O_2$ mixtures (Fig. 5c), $\Delta H^{*\ddagger}_{app,epox}$ may decrease with increasing x_{H_2O} because the transition state needs to displace a smaller quantity of bulky $C_4H_6O_2$ molecules, offsetting the enthalpic penalty of disrupting hydrogen bonded solvent molecules and reducing $H^{\ddagger,\varepsilon}_{epox}$.

Fig. 6 demonstrates that values of $\Delta H^{*\ddagger}_{app,decomp}$ also depend strongly on x_{H_2O} in each organic solvent. $\Delta H^{*\ddagger}_{app,decomp}$ decreases with increasing x_{H_2O} in both Ti-BEA-OH and Ti-BEA-F because greater quantities of H_2O near sites enthalpically stabilize the hydrophilic transition state for H_2O_2 decomposition more significantly than Ti–OOH (Scheme 3b). For a given organic solvent and x_{H_2O}, Ti-BEA-F gives greater $\Delta H^{*\ddagger}_{app,decomp}$ values than Ti-BEA-OH. More H_2O molecules may adsorb and hydrogen bond with the transition state within Ti-BEA-OH, which yields lower $H^{\ddagger,\varepsilon}_{decomp}$ values. $\Delta H^{*\ddagger}_{app,decomp}$ depends more strongly on x_{H_2O} for Ti-BEA-OH than Ti-BEA-F in each organic solvent, showing that x_{H_2O} affects the stability of

Fig. 6 $\Delta H^{*\ddagger}_{app,decomp}$ values for H_2O_2 decomposition (1 mM H_2O_2, 313–343 K) as a function of x_{H_2O} in mixtures of (a) CH_3OH (■,□), (b) CH_3CN (■,□), and (c) $C_4H_6O_2$ (■,□) with H_2O over Ti-BEA-OH (solid) and Ti-BEA-F (hollow).

adsorbed reactive species more significantly in Ti-BEA-OH than Ti-BEA-F. Between organic solvents, $\Delta H^{*\ddagger}_{\text{app,decomp}}$ values differ by 4 kJ mol^{-1} over Ti-BEA-F and 8 kJ mol^{-1} over Ti-BEA-OH at the highest x_{H_2O} (0.75). The smaller changes observed in Ti-BEA-F imply that H_2O molecules form similar first coordination solvation shells around the transition state and Ti–OOH intermediate at the highest x_{H_2O}. In contrast, the differences among Ti-BEA-OH may reflect contributions from extended hydrogen bonding networks of H_2O and organic solvent molecules within Ti-BEA-OH that influence both the decomposition transition state and Ti–OOH intermediate. $\Delta H^{*\ddagger}_{\text{app,epox}}$ values differ by 6 kJ mol^{-1} for Ti-BEA-F and 26 kJ mol^{-1} over Ti-BEA-OH at the highest x_{H_2O} values, and the spans of values and differences between zeolites exceed that for $\Delta H^{*\ddagger}_{\text{app,decomp}}$. This finding agrees with chemical intuition that the larger transition state for C_6H_{12} epoxidation depends more sensitively on the secondary coordination sphere of solvent molecules within the pore than the smaller transition state for H_2O_2 decomposition (Scheme 3). Recent work demonstrated that solvent displacement dominates $\Delta H_{\text{app,epox}}$ differences as a function of alkene carbon number in aqueous CH_3CN, suggesting that changes in $(SiOH)_x$ and intrapore solvent composition more significantly affect the stability of larger transition states that displace more solvent.[34]

The differences in the functional dependencies of $\Delta H^{*\ddagger}_{\text{app,decomp}}$ and $\Delta H^{*\ddagger}_{\text{app,epox}}$ on x_{H_2O} must reflect differences in the hydrophilicity of the transition state complexes for these competing reaction pathways. Greater x_{H_2O} may increase H^ε of the hydrophobic transition state for epoxidation from a combination of increased disruption of H_2O molecules and unfavorable interactions between the transition state and intrapore H_2O. In contrast, greater quantities of H_2O molecules likely lower H^ε for the transition state for H_2O_2 decomposition in all organic solvents. Among organic solvents, changing x_{H_2O} in CH_3OH mixtures has the least significant effect on both $\Delta H^{*\ddagger}_{\text{app,epox}}$ and $\Delta H^{*\ddagger}_{\text{app,decomp}}$ values. The weak effects of x_{H_2O} in CH_3OH likely reflect the more similar hydrogen bonding ability of CH_3OH to H_2O than CH_3CN or $C_4H_6O_2$ (see Section S10† for solvent parameters). Therefore, CH_3OH molecules may hydrogen bond with reactive species in the pore similarly to H_2O, which lessens the differences in the solvent organization within pores brought about by replacing a fraction of CH_3OH with H_2O.

Overall, activation barrier measurements for epoxidation and H_2O_2 decomposition in Fig. 5 and 6 suggest that the organic solvent, x_{H_2O}, and $(SiOH)_x$ density in Ti-BEA affect the stability of the Ti–OOH intermediate and transition states for epoxidation and H_2O_2 decomposition. The differences in stability result from differences between the organization and composition of fluid-like molecules within Ti-BEA pores, as described next.

3.5 Intrapore solvent composition depends on bulk solvent composition and $(SiOH)_x$ density

The bulk solvent composition[79,88,89] and intrapore $(SiOH)_x$ density[90–92] affect the intrapore composition of solvent molecules and other adsorbates in aqueous-organic solvent mixtures. Fig. 7 presents measured mole fractions of H_2O within pores $(x_{H_2O,\text{pore}})$ (see Section S2†) in equilibrated mixtures of H_2O with CH_3CN, CH_3OH, and $C_4H_6O_2$ as a function of the bulk H_2O fraction $(x_{H_2O,\text{bulk}})$. For each organic solvent and zeolite, increasing $x_{H_2O,\text{bulk}}$ leads to greater $x_{H_2O,\text{pore}}$ values across the full range of conditions examined. These observations agree with the interpretations of changes in turnover rates and activation parameters as functions of x_{H_2O} (Sections 3.1 and 3.4) and explains how altering $x_{H_2O,\text{bulk}}$ influences the stabilities of reactive species both in the bulk (i.e., C_6H_{12} and H_2O_2) and in pores (i.e., Ti–OOH and transition states). Ti-BEA-OH adsorbs a greater fraction of H_2O than Ti-BEA-F for all combinations of organic solvents and $x_{H_2O,\text{bulk}}$, consistent with vapor adsorption results (Fig. S8a†) that show $(SiOH)_x$ groups promote H_2O adsorption. The ratio of $x_{H_2O,\text{pore}}$ between Ti-BEA-OH and Ti-BEA-F generally decreases as $x_{H_2O,\text{bulk}}$ increases. This suggests that $(SiOH)_x$ functions carry a stronger influence on H_2O adsorption at low $x_{H_2O,\text{bulk}}$, because the pores contain fewer H_2O molecules. This interpretation agrees with previously published binary adsorption measurements that indicate values of $x_{H_2O,\text{pore}}$ in hydrophilic zeolites depend more strongly on $x_{H_2O,\text{bulk}}$ from mixtures with methanol,[93] ethanol,[94,95] and acetic acid[96] at lower $x_{H_2O,\text{bulk}}$ values. As $x_{H_2O,\text{bulk}}$ increases, H_2O molecules associate with H_2O already within pores, which leads to a weaker influence of the $(SiOH)_x$ density and organic co-solvent on adsorption. This explanation agrees with CH_3CN mixtures that give the greatest difference in $x_{H_2O,\text{pore}}$ between zeolites at low $x_{H_2O,\text{bulk}}$. CH_3CN contains a lower sum of hydrogen bond donors and acceptors (1) than CH_3OH (3) or $C_4H_6O_2$ (4) (Scheme S1†), as such, CH_3CN molecules offer fewer sites for H_2O molecules to associate than other organic solvents. Furthermore, CH_3CN mixtures give greater uptakes of H_2O within Ti-BEA-OH than the other organic solvents at similar $x_{H_2O,\text{bulk}}$. CH_3OH and $C_4H_6O_2$ may interact with $(SiOH)_x$ more strongly than CH_3CN, which suggests those molecules may compete with H_2O for $(SiOH)_x$ sites more effectively than CH_3CN. The bulky nature of $C_4H_6O_2$ may also lead to a lower available pore volume for H_2O molecules to co-adsorb.

For all organic solvents, Ti-BEA-OH shows greater $x_{H_2O,\text{pore}}$ values than Ti-BEA-F, and an increase in $x_{H_2O,\text{bulk}}$ leads to a corresponding increase in $x_{H_2O,\text{pore}}$. These observations correspond to our interpretations of the effect of x_{H_2O} on C_6H_{12} epoxidation and H_2O_2 decomposition, as outlined in the previous sections. While Fig. 7 demonstrates that Ti-BEA-OH promotes a more H_2O-rich pore solvent environment (higher $x_{H_2O,\text{pore}}$), the vapor adsorption isotherms from Fig. 8a also suggest that Ti-BEA-OH likely adsorbs greater numbers of H_2O molecules. Ti-BEA-OH adsorbs a greater volume of H_2O than Ti-BEA-F at all P/P_0 values, with the largest difference between the zeolites ($\sim$10-fold) occurring at 0.5 $P_{H_2O}/P_{H_2O,0}$. The greater H_2O uptake in Ti-BEA-OH agrees with previous vapor H_2O adsorption measurements over MFI[42,97,98] and *BEA[27,43,48] zeolites that observed increasing H_2O uptake with increasing $(SiOH)_x$ density. Furthermore, the isotherm in Fig. 8b signifies that Ti-BEA-OH preferentially adsorbs CH_3OH molecules, with the maximum difference between Ti-BEA-OH and Ti-BEA-F ($\sim$3.5-fold) at 0.03 $P_{CH_3OH}/P_{CH_3OH,0}$. The H_2O and CH_3OH uptake in Ti-

Fig. 7 Intrapore mole fraction of H_2O ($x_{H_2O,pore}$) as a function of the equilibrium bulk H_2O fraction ($x_{H_2O,bulk}$) at 313 K in mixtures of (a) CH_3OH (■,□), (b) CH_3CN (■,□), and (c) $C_4H_6O_2$ (■,□) with H_2O over Ti-BEA-OH (solid points) and Ti-BEA-F (hollow points). The faint green lines signify the parity line.
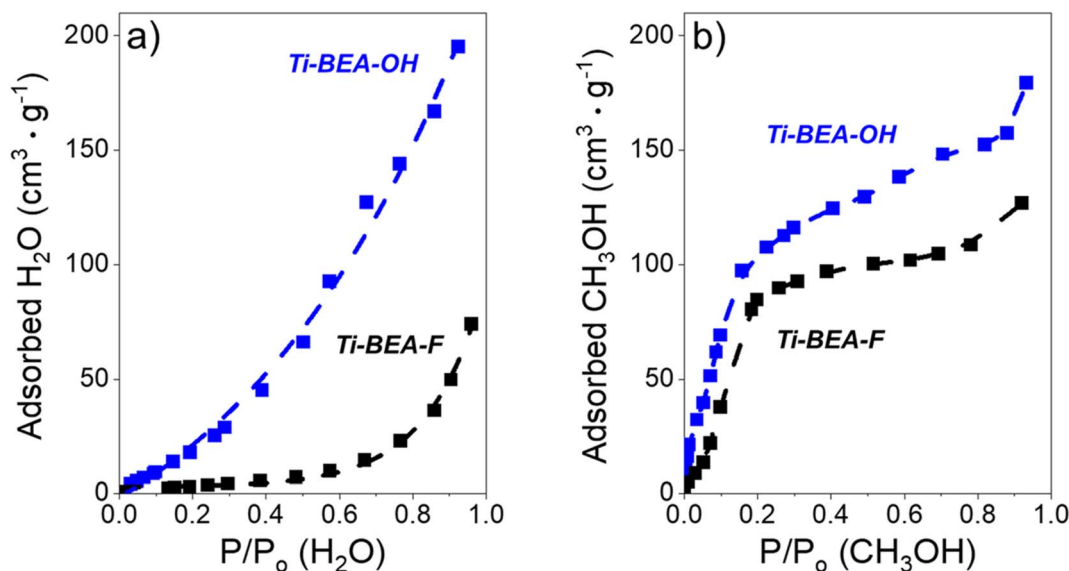

Fig. 8 (a) H_2O (295 K) and (b) CH_3OH (295 K) adsorption isotherms over Ti-BEA-OH (blue) and Ti-BEA-F (black). The samples were degassed at 673 K under vacuum (<0.7 Pa) before adsorption.

BEA-OH exceeds Ti-BEA-F by more than 3 and 1.3 times, respectively, at all P/P_0 values greater than 0.01, which cannot stem from the differences between BET surface areas and pore volumes in Table 1. The experimental capabilities of the vapor adsorption instrument prohibit measurements with CH_3CN and $C_4H_6O_2$. Nevertheless, these observations provide strong evidence that $(SiOH)_x$ defects promote the uptake of molecules with hydrogen bonding functions, an interpretation supported by prior infrared spectroscopy experiments and molecular dynamics simulations showing that Ti-BEA-OH adsorbs more CH_3CN molecules than Ti-BEA-F.[34] Therefore, Ti-BEA-OH likely

contains greater quantities of both H_2O and the organic co-solvent (*i.e.*, CH_3CN, CH_3OH, $C_4H_6O_2$) at all conditions, which leads to higher solvent densities within pores. These differences in intrapore solvent densities lead to greater C_6H_{12} epoxidation turnover rates through displacement and reorganization of hydrogen bonded solvent molecules, as reported for CH_3CN.[34]

More generally, the data in Fig. 7 and 8 demonstrate that the solvent composition and density within porous catalysts can be tuned by altering the bulk composition and catalyst $(SiOH)_x$ density. This knowledge allows for control of the intrapore and bulk solvent environment for any liquid phase chemistry, which

can significantly influence rates and selectivities for catalysis and adsorption processes.

3.6 Measured enthalpies for adsorption and activation reveal influence of intrapore solvents on surface species

Brønsted–Evans–Polanyi relations propose that the intrinsic activation energy for an elementary step scales linearly with the enthalpy of reaction for the same process.[99–101] Hammond postulated that the transition state structurally resembles the reaction state (*i.e.*, reactant or product) most similar in energy, which leads to strong correlations between reaction kinetics and thermodynamics for adsorption of reactant or product molecules, as demonstrated frequently on metal surfaces and in computation.[102,103] Recently, the validity of these concepts were demonstrated within solvent-filled pore of zeolite catalysts used for alkene epoxidations. Values of $\Delta H^{\ddagger}_{\text{app,epox}}$ correlate with the liquid phase enthalpy of epoxide adsorption ($\Delta H_{\text{ads,epox}}$) for C_6H_{12} epoxidation and $C_6H_{12}O$ adsorption over *BEA zeolites containing different active metals (*i.e.*, Ti, Nb, W)[58] and C_6–C_{18} alkenes and epoxides over Ti-BEA with varying (SiOH)$_x$ densities.[28,34] The positive correlations between the enthalpies in these previous studies indicate that the transition state for epoxidation structurally resembles the adsorbed epoxidation product (Scheme 3a), because excess enthalpy contributions from interactions with surrounding solvent molecules affect epoxide adsorption and epoxidation transition state formation similarly. Measuring differences in $\Delta H_{\text{ads,epox}}$ provides a complementary method to examine how the composition of the organic solvent, $x_{\text{H}_2\text{O}}$, and (SiOH)$_x$ density of Ti-BEA catalysts impact the structure of intrapore solvation structures and their influence on the stability of surface intermediates.

Isothermal titration calorimetry (ITC) experiments provided values of $\Delta H_{\text{ads,epox}}$ for $C_6H_{12}O$. The calorimeter releases heat upon each injection of $C_6H_{12}O$ solution into a solution of Ti-

BEA, as shown in a representative ITC thermogram in Fig. 9a. Fig. 9b shows the molar heats of adsorption from Fig. 9a at low $C_6H_{12}O$ coverages (<0.25 mol $C_6H_{12}O$ (mol Ti)$^{-1}$), a regime in which all epoxide molecules are assumed to adsorb to Ti sites.[28] Values of $\Delta H_{\text{ads,epox}}$ for 1,2-epoxyhexane within each combination of solvent and Ti-BEA zeolite were calculated from the average value of the heat released in this low coverage regime. The first injection (transparent) was omitted from the $\Delta H_{\text{ads,epox}}$ calculation, because these values exhibit much lower heat than other points due to well-known instrumental errors (*e.g.*, evaporation of titrant from syringe needle, leading to smaller than expected injected volumes). The thermograms and integrated heat data for the remaining solvent combinations and zeolites are found in Section S11.†

Fig. 10a displays $\Delta H_{\text{ads,epox}}$ values for $C_6H_{12}O$ as a function of $x_{\text{H}_2\text{O}}$. Notably, aqueous CH_3CN mixtures and neat CH_3CN give significantly more exothermic $\Delta H_{\text{ads,epox}}$ values than either CH_3OH or $C_4H_6O_2$ solutions, which suggests that CH_3CN mixtures provide the greatest stability to adsorbed $C_6H_{12}O$. These comparisons appear to explain why CH_3CN mixtures show greater C_6H_{12} epoxidation turnover rates (Fig. 1) than the other solvents examined. Fig. 10b shows that $\Delta H_{\text{ads,epox}}$ values correlate with $\Delta H^{*\ddagger}_{\text{app,epox}}$ values across all combinations of solvent composition and zeolites, which signifies the strong structural similarities between the intrapore solvation environment of 1,2-epoxyhexane bound to Ti active sites and the transition states for epoxidation that form in these same environments. The dependence of $\Delta H^{*\ddagger}_{\text{app,epox}}$ and $\Delta H_{\text{ads,epox}}$ on $x_{\text{H}_2\text{O}}$ is weaker over Ti-BEA-F than Ti-BEA-OH (see Fig. 5 and 10a) for all solvents, which shows that increases in $x_{\text{H}_2\text{O}}$ lead to less significant changes in the solvent structure within Ti-BEA-F (see Section 3.5). Based on insight gained from quantitative comparisons between GCMD simulations and ITC measurements of $\Delta H_{\text{ads,epox}}$ values,[34] the more endothermic $\Delta H^{*\ddagger}_{\text{app,epox}}$
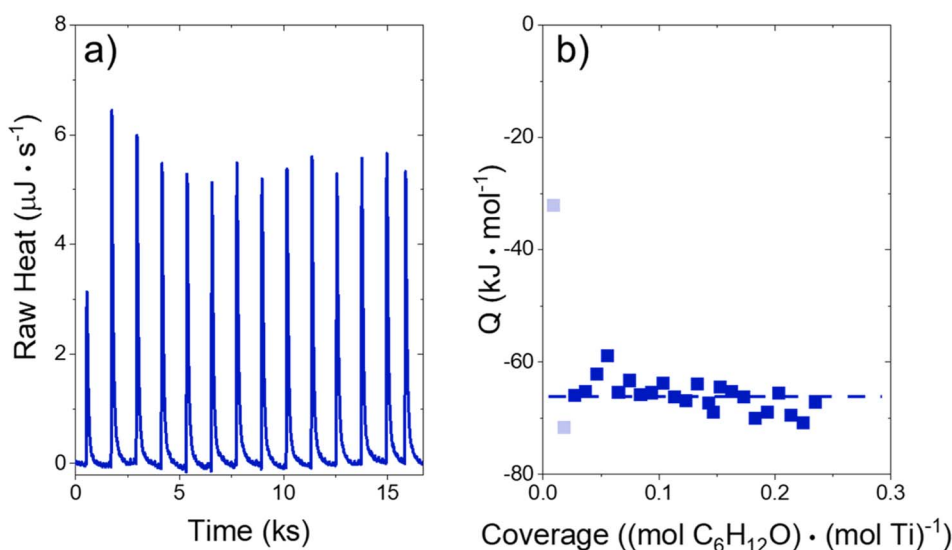

Fig. 9 (a) Thermogram from the titration of Ti-BEA-OH with 1,2-epoxyhexane (10 mM $C_6H_{12}O$ in $x_{C_4H_6O_2}$ = 0.25 (7.6 M) with H_2O (22.8 M), 313 K, 1 μL per injection) during isothermal titration calorimetry (ITC), and (b) the corresponding heats released as a function of 1,2-epoxyhexane coverage. Transparent points are omitted due to common errors associated with early injections.

Fig. 10 (a) $C_6H_{12}O$ enthalpies of adsorption (5–10 mM $C_6H_{12}O$, 313 K) as a function of x_{H_2O} and (b) difference between the enthalpy of the transition state for C_6H_{12} epoxidation (1 mM C_6H_{12}, 308–333 K) and the Ti–OOH and standard state C_6H_{12} enthalpies as a function of $C_6H_{12}O$ enthalpies of adsorption (5–10 mM $C_6H_{12}O$, 313 K) in aqueous mixtures of (a) CH_3OH (■,□), (b) CH_3CN (■, □), and (c) $C_4H_6O_2$ (■,□) over Ti-BEA-OH (solid points) and Ti-BEA-F (hollow points).

and $\Delta H_{ads,epox}$ values in CH_3CN mixtures at higher x_{H_2O} reflect the disruptions of greater numbers of hydrogen bonds that involve H_2O molecules upon adsorption of the epoxide. Presumably, the changes of $\Delta H^{*\ddagger}_{app,epox}$ and $\Delta H_{ads,epox}$ with x_{H_2O} in CH_3OH mixtures over Ti-BEA-OH reflect similar processes that displace solvent molecules, however, the lower magnitude of these changes in CH_3OH likely stems from the greater hydrogen bonded character of neat CH_3OH relative to neat CH_3CN. Hence, the addition of small quantities of H_2O leads to more significant changes in the organization of CH_3CN molecules within pores than CH_3OH. In contrast, the values of $\Delta H^{*\ddagger}_{app,epox}$ and $\Delta H_{ads,epox}$ become more exothermic with increasing x_{H_2O} in $C_4H_6O_2$ mixtures. While the full reasons for this trend remain unclear presently, these results give evidence that the spatial positioning of $C_4H_6O_2$ within pores responds to the presence of water.

Notably, $\Delta H^{*\ddagger}_{app,epox}$ and $\Delta H_{ads,epox}$ show a positive and super-linear correlation for every combination of solvent and zeolite (Fig. 9b). The derivative of the correlation increases at more endothermic enthalpies, which indicates that the transition state for epoxidation resembles the epoxide product more closely at more endothermic $\Delta H^{*\ddagger}_{app,epox}$ values, following Hammond's postulate.[102] We cannot, however, exclude the possibility that H_{Ti-OOH}^{ε} varies systematically with x_{H_2O} and contributes to the non-linear trend. Nevertheless, the positive correlations between $\Delta H^{*\ddagger}_{app,epox}$ and $\Delta H_{ads,epox}$ suggests that interactions with solvent molecules affect the stability of the epoxidation transition state and the adsorbed epoxide in

similar ways. These findings show that solvent molecules and solvent composition influence the stability of solutes in bulk solvents and at solid–liquid interfaces during catalysis. These concepts can guide the design of not only heterogeneously catalyzed reactions, but also liquid phase homogeneously catalyzed and organic reactions in which reactant γ values carry significance.

4. Conclusions

The organic solvent choice, x_{H_2O}, and zeolite $(SiOH)_x$ density influence rates and selectivities of liquid phase zeolite-catalyzed reactions by altering G^{ε} values of reactants in the bulk fluid phase and at solid–liquid interfaces, as demonstrated with interpretations of alkene epoxidation kinetics. While the organic solvent identity and x_{H_2O} influence the reversibility of H_2O_2 activation, neither the solvent nor zeolite choice influences the mechanisms for alkene epoxidation or H_2O_2 decomposition. Instead, differences among turnover rates and selectivities stem from the distinct dependence of G^{ε} values of reactive species for C_6H_{12} epoxidation and H_2O_2 decomposition on x_{H_2O}. Greater rates of C_6H_{12} epoxidation in each zeolite and organic solvent at greater x_{H_2O} appear to be primarily driven by incommensurate changes in the activity coefficients of C_6H_{12} and for epoxidation transition states. However, H_2O_2 decomposition rates decrease at higher x_{H_2O} for both Ti-BEA-OH and Ti-BEA-F, likely because stabilization of the hydrophilic transition state by H_2O is outweighed by the stabilization of fluid phase H_2O_2 and the Ti–OOH intermediate.

The findings reported here demonstrate the significance of interactions between solvent molecules and reactants in the liquid phase and at solid–liquid interfaces during catalytic reactions. Broadly, the findings suggest that introducing a more polar reaction environment promotes zeolite-catalyzed reaction pathways with predominantly hydrophobic reactants and transition states while suppressing pathways with hydrophilic reactive species. For industrial purposes, diluting organic solvents with H_2O increases separation costs for epoxidation, may increase rates of ring-opening of the epoxide product[40,104,105] (not observed under differential conversions in this study), and may influence the long-term stability of zeolite catalysts.[106–108] Results presented here show that simply adding more H_2O increases rates and H_2O_2 selectivities for C_6H_{12} epoxidation in confined environments. Evidently, proper selection of organic solvent, x_{H_2O}, and catalyst polarity and topology can improve the performance of liquid phase reactions. The concepts outlined here can guide the design of adsorption and catalytic processes in the liquid phase and at solid–liquid interfaces.

Data availability

Characterization plots, supplemental kinetics and UV-Vis spectra, full rate derivations, activity coefficient values, activation barriers, tabulated solvent parameters, and all calorimetry thermograms have been included as part of the ESI.†

Author contributions

D. S. P. synthesized and characterized the zeolites, performed the NMR and UV-Vis spectroscopy experiments, and conducted measurements of rates and enthalpies of adsorption. C. T. performed the vapor H_2O and CH_3OH adsorption measurements. O. K. assisted with the kinetic measurements and synthesis of zeolites. D. W. F. conceptualized the manuscript. The manuscript was written by D. S. P. with input from all authors. All authors have given approval to the final version of the manuscript.

Conflicts of interest

There are no conflicts to declare.

Acknowledgements

Notes and references

1 S. T. Oyama, Rates, Kinetics, and Mechanisms of Epoxidation, in *Mechanisms in Homogeneous and Heterogeneous Epoxidation Catalysis*, Elsevier, 2008, pp. 3–99.

2 Degussa AG and Uhde GmbH, Process for the epoxidation of propene, *WO Pat.*, WO 2005/000827A1, 2005.

3 BASF SE and Dow Global Technologies LLC, Process for preparing propylene oxide, *US Pat.*, US10435381B2, 2019.

4 Lyondell Chemical Technology LP, Process for the preparation of propylene oxide, *EP Pat.*, EP1742928B1, 2011.

5 BASF SE, Process for the preparation of propylene oxide, *US Pat.*, US10544115B2, 2020.

6 BASF SE and Dow Global Technologies LLC, Catalyst system for preparing propylene oxide, *US Pat.*, US10053439B2, 2018.

7 Sumitomo Chemical Company, Limited, Method for producing propylene oxide, *WO Pat.*, WO2009/008493A2, 2009.

8 M. A. Mellmer, C. Sener, J. M. Gallo, J. S. Luterbacher, D. M. Alonso and J. A. Dumesic, Solvent effects in acid-catalyzed biomass conversion reactions, *Angew. Chem., Int. Ed.*, 2014, **53**(44), 11872–11875.

9 M. A. Mellmer, C. Sanppitsekree, B. Demir, P. Bai, K. Ma, M. Neurock and J. A. Dumesic, Solvent-Enabled Control of Reactivity for Liquid Phase Reactions of Biomass-Derived Compounds, *Nat. Catal.*, 2018, **1**, 199–207.

10 T. W. Walker, A. K. Chew, H. Li, B. Demir, Z. C. Zhang, G. W. Huber, R. C. Van Lehn and J. A. Dumesic, Universal kinetic solvent effects in acid-catalyzed reactions of biomass-derived oxygenates, *Energy Environ. Sci.*, 2018, **11**(3), 617–628.

11 M. A. Mellmer, J. M. R. Gallo, D. Martin Alonso and J. A. Dumesic, Selective Production of Levulinic Acid from Furfuryl Alcohol in THF Solvent Systems over H-ZSM-5, *ACS Catal.*, 2015, **5**(6), 3354–3359.

12 C. Sievers, Y. Noda, L. Qi, E. M. Albuquerque, R. M. Rioux and S. L. Scott, Phenomena Affecting Catalytic Reactions at Solid–Liquid Interfaces, *ACS Catal.*, 2016, **6**(12), 8286–8307.

13 G. Li, B. Wang and D. E. Resasco, Water-Mediated Heterogeneously Catalyzed Reactions, *ACS Catal.*, 2020, **10**(2), 1294–1309.

14 D. S. Potts, D. T. Bregante, J. S. Adams, C. Torres and D. W. Flaherty, Influence of solvent structure and hydrogen bonding on catalysis at solid–liquid interfaces, *Chem. Soc. Rev.*, 2021, **50**(22), 12308–12337.

15 J. S. Bates and R. Gounder, Kinetic effects of molecular clustering and solvation by extended networks in zeolite acid catalysis, *Chem. Sci.*, 2021, **12**(13), 4699–4708.

16 G. Li, B. Wang and D. E. Resasco, Solvent effects on catalytic reactions and related phenomena at liquid–solid interfaces, *Surf. Sci. Rep.*, 2021, **76**(4), 100541.

17 J. Trouvé and R. Gramage-Doria, Beyond hydrogen bonding: recent trends of outer sphere interactions in transition metal catalysis, *Chem. Soc. Rev.*, 2021, **50**(5), 3565–3584.

18 M. Raynal, P. Ballester, A. Vidal-Ferran and P. W. van Leeuwen, Supramolecular catalysis. Part 1: non-covalent interactions as a tool for building and modifying homogeneous catalysts, *Chem. Soc. Rev.*, 2014, **43**(5), 1660–1733.

19 P. J. Dyson and P. G. Jessop, Solvent effects in catalysis: rational improvements of catalysts *via* manipulation of solvent interactions, *Catal. Sci. Technol.*, 2016, **6**(10), 3302–3316.

20 D. N. Silverman and R. McKenna, Solvent-mediated proton transfer in catalysis by carbonic anhydrase, *Acc. Chem. Res.*, 2007, **40**(8), 669–675.

21 C. Reichardt and T. Welton, *Solvents and solvent effects in organic chemistry*, John Wiley & Sons, 2011.

22 N. Menschutkin, Über die Affinitätskoeffizienten der Alkylhaloide und der Amine, *Z. Phys. Chem.*, 1890, **6**(1), 41.

23 J. G. Kirkwood, Theory of Solutions of Molecules Containing Widely Separated Charges with Special Application to Zwitterions, *J. Chem. Phys.*, 1934, **2**(7), 351–361.

24 P. Debye and E. Hückel, Zur Theorie der Elektrolyte. I. Gefrierpunktserniedrigung und verwandte Erscheinungen, *Phys. Z.*, 1923, **24**(9), 185–206.

25 M. J. Kamlet, J. L. M. Abboud, M. H. Abraham and R. W. Taft, Linear solvation energy relationships. 23. A comprehensive collection of the solvatochromic parameters,.pi.*,.alpha., and.beta., and some methods for simplifying the generalized solvatochromic equation, *J. Org. Chem.*, 1983, **48**(17), 2877–2887.

26 R. J. Madon and E. Iglesia, Catalytic reaction rates in thermodynamically non-ideal systems, *J. Mol. Catal. A: Chem.*, 2000, **163**(1–2), 189–204.

27 D. T. Bregante, A. M. Johnson, A. Y. Patel, E. Z. Ayla, M. J. Cordon, B. C. Bukowski, J. Greeley, R. Gounder and D. W. Flaherty, Cooperative Effects between Hydrophilic Pores and Solvents: Catalytic Consequences of Hydrogen Bonding on Alkene Epoxidation in Zeolites, *J. Am. Chem. Soc.*, 2019, **141**, 7302–7319.

28 D. T. Bregante and D. W. Flaherty, Impact of Specific Interactions Among Reactive Surface Intermediates and Confined Water on Epoxidation Catalysis and Adsorption in Lewis Acid Zeolites, *ACS Catal.*, 2019, **9**(12), 10951–10962.

29 J. Z. Tan, D. T. Bregante, C. Torres and D. W. Flaherty, Transition state stabilization depends on solvent identity, pore size, and hydrophilicity for epoxidations in zeolites, *J. Catal.*, 2022, **405**, 91–104.

30 L. Wu, Z. Tang, Y. Yu, X. Yao, W. Liu, L. Li, B. Yan, Y. Liu and M. He, Facile synthesis of a high-performance titanosilicate catalyst with controllable defective Ti(OSi)$_3$OH sites, *Chem. Commun.*, 2018, **54**(49), 6384–6387.

31 Z. Tang, Y. Yu, W. Liu, Z. Chen, R. Wang, H. Liu, H. Wu, Y. Liu and M. He, Deboronation-assisted construction of defective Ti(OSi)$_3$OH species in MWW-type titanosilicate

and their enhanced catalytic performance, *Catal. Sci. Technol.*, 2020, **10**(9), 2905–2915.

32 L. Wang, J. Sun, X. Meng, W. Zhang, J. Zhang, S. Pan, Z. Shen and F.-S. Xiao, A significant enhancement of catalytic activities in oxidation with H$_2$O$_2$ over the TS-1 zeolite by adjusting the catalyst wettability, *Chem. Commun.*, 2014, **50**(16), 2012–2014.

33 D. T. Bregante, M. C. Chan, J. Z. Tan, E. Z. Ayla, C. P. Nicholas, D. Shukla and D. W. Flaherty, The shape of water in zeolites and its impact on epoxidation catalysis, *Nat. Catal.*, 2021, **4**(9), 797–808.

34 D. S. Potts, V. S. Jeyaraj, O. Kwon, R. Ghosh, A. V. Mironenko and D. W. Flaherty, Effect of Interactions between Alkyl Chains and Solvent Structures on Lewis Acid Catalyzed Epoxidations, *ACS Catal.*, 2022, **12**(21), 13372–13393.

35 C. Ramachandran, H. Du, Y. Kim, M. Kung, R. Snurr and L. Broadbelt, Solvent effects in the epoxidation reaction of 1-hexene with titanium silicalite-1 catalyst, *J. Catal.*, 2008, **253**(1), 148–158.

36 G. Langhendries, D. E. De Vos, G. V. Baron and P. A. Jacobs, Quantitative Sorption Experiments on Ti-Zeolites and Relation with α-Olefin Oxidation by H2O2, *J. Catal.*, 1999, **187**(2), 453–463.

37 W. Fan, P. Wu and T. Tatsumi, Unique solvent effect of microporous crystalline titanosilicates in the oxidation of 1-hexene and cyclohexene, *J. Catal.*, 2008, **256**(1), 62–73.

38 J. C. Van Der Waal and H. Van Bekkum, Zeolite titanium beta: a versatile epoxidation catalyst. Solvent effects, *J. Mol. Catal. A: Chem.*, 1997, **124**(2–3), 137–146.

39 A. Corma, P. Esteve and A. Martínez, Solvent Effects during the Oxidation of Olefins and Alcohols with Hydrogen Peroxide on Ti-Beta Catalyst: The Influence of the Hydrophilicity-Hydrophobicity of the Zeolite, *J. Catal.*, 1996, **161**, 11–19.

40 F. Song, Y. M. Liu, L. L. Wang, H. J. Zhang, M. Y. He and P. Wu, Highly efficient epoxidation of propylene over a novel Ti-MWW catalyst, *Stud. Surf. Sci. Catal.*, 2007, **170**, 1236–1243.

41 J. Yin, H. Xu, B. Wang, W. Tian, J. Yin, J. Jiang and P. Wu, Highly selective 1-pentene epoxidation over Ti-MWW with modified microenvironment of Ti active sites, *Catal. Sci. Technol.*, 2020, **10**(17), 6050–6064.

42 D. T. Bregante, D. S. Potts, O. Kwon, E. Z. Ayla, J. Z. Tan and D. W. Flaherty, Effects of Hydrofluoric Acid Concentration on the Density of Silanol Groups and Water Adsorption in Hydrothermally Synthesized Transition-Metal-Substituted Silicalite-1, *Chem. Mater.*, 2020, **32**(17), 7425–7437.

43 R. Gounder and M. E. Davis, Beyond shape selective catalysis with zeolites: hydrophobic void spaces in zeolites enable catalysis in liquid water, *AIChE J.*, 2013, **59**(9), 3349–3358.

44 V. V. Potekhin, V. A. Kulikova, E. G. Kochina and V. M. Potekhin, Decomposition of hydrogen peroxide in protic and polar aprotic solvents on TS-1 heterogeneous catalyst, *Russ. J. Appl. Chem.*, 2011, **84**(7), 1195–1200.

45 P. Wolf, C. Hammond, S. Conrad and I. Hermans, Post-synthetic preparation of Sn-, Ti- and Zr-beta: a facile route to water tolerant, highly active Lewis acidic zeolites, *Dalton Trans.*, 2014, **43**(11), 4514–4519.

46 D. T. Bregante, P. Priyadarshini and D. W. Flaherty, Kinetic and spectroscopic evidence for reaction pathways and intermediates for olefin epoxidation on Nb in *BEA, *J. Catal.*, 2017, **348**, 75–89.

47 T. Blasco, M. A. Camblor, A. Corma, P. Esteve, J. M. Guil, A. Martinez, J. A. Perdigon-Melon and S. Valencia, Direct synthesis and characterization of hydrophobic aluminum-free Ti-beta zeolite, *J. Phys. Chem. B*, 1998, **102**, 75–88.

48 M. J. Cordon, J. W. Harris, J. C. Vega-Vila, J. S. Bates, S. Kaur, M. Gupta, M. E. Witzke, E. C. Wegener, J. T. Miller, D. W. Flaherty, D. D. Hibbitts and R. Gounder, Dominant Role of Entropy in Stabilizing Sugar Isomerization Transition States within Hydrophobic Zeolite Pores, *J. Am. Chem. Soc.*, 2018, **140**(43), 14244–14266.

49 J. M. Newsam, M. M. J. Treacy, W. T. Koetsier and C. B. D. Gruyter, Structural characterization of zeolite beta, *Proc. R. Soc. London, Ser. A*, 1988, **420**(1859), 375–405.

50 B. S. Shirke, P. V. Korake, P. P. Hankare, S. R. Bamane and K. M. Garadkar, Synthesis and characterization of pure anatase TiO₂ nanoparticles, *J. Mater. Sci.: Mater. Electron.*, 2011, **22**(7), 821–824.

51 J. Rouquerol, P. Llewellyn and F. Rouquerol, Is the BET equation applicable to microporous adsorbents?, in *Studies in Surface Science and Catalysis*, Elsevier, Amsterdam and Oxford, 2007, vol. 160, pp. 49–56.

52 A. Galarneau, F. Villemot, J. Rodriguez, F. Fajula and B. Coasne, Validity of the t-plot Method to Assess Microporosity in Hierarchical Micro/Mesoporous Materials, *Langmuir*, 2014, **30**(44), 13266–13274.

53 J. Wang, V. F. Kispersky, W. N. Delgass and F. H. Ribeiro, Determination of the Au active site and surface active species *via* operando transmission FTIR and isotopic transient experiments on 2.3 wt% Au/TiO₂ for the WGS reaction, *J. Catal.*, 2012, **289**, 171–178.

54 A. Zecchina, S. Bordiga, G. Spoto, L. Marchese, G. Petrini, G. Leofanti and M. Padovan, Silicalite characterization. 2. IR spectroscopy of the interaction of carbon monoxide with internal and external hydroxyl groups, *J. Phys. Chem.*, 1992, **96**(12), 4991–4997.

55 S. Dzwigaj, M. J. Peltre, P. Massiani, A. Davidson, M. Che, S. Dzwigaj, P. Massiani, T. Sen and S. Sivasanker, Incorporation of vanadium species in a dealuminated β zeolite, *Chem. Commun.*, 1998, (1), 87–88.

56 A. Jentys and J. Lercher, Techniques of zeolite characterization, in *Studies in Surface Science and Catalysis*, Elsevier, 2001, vol. 137, pp. 345–386.

57 I. Chorkendorff and J. W. H. Niemantsverdriet, *Concepts of Modern Catalysis and Kinetics*, Wiley-VCH Verlag Gmbh & Co., Weinheim, 2nd edn, 2007, pp. 203–214.

58 E. Z. Ayla, D. S. Potts, D. T. Bregante and D. W. Flaherty, Alkene Epoxidations with H₂O₂ over Groups 4–6 Metal-Substituted BEA Zeolites: Reactive Intermediates,

Reaction Pathways, and Linear Free-Energy Relationships, *ACS Catal.*, 2021, **11**(1), 139–154.

59 D. T. Bregante and D. W. Flaherty, Periodic Trends in Olefin Epoxidation over Group IV and V Framework-Substituted Zeolite Catalysts: A Kinetic and Spectroscopic Study, *J. Am. Chem. Soc.*, 2017, **139**(20), 6888–6898.

60 E. Z. Ayla, D. Patel, A. Harris and D. W. Flaherty, Identity of the Metal Oxide Support Controls Outer Sphere Interactions that Change Rates and Barriers for Alkene Epoxidations at Isolated Ti Atoms, *J. Catal.*, 2022, **411**, 167–176.

61 D. T. Bregante, J. Z. Tan, R. L. Schultz, E. Z. Ayla, D. S. Potts, C. Torres and D. W. Flaherty, Catalytic Consequences of Oxidant, Alkene, and Pore Structures on Alkene Epoxidations within Titanium Silicates, *ACS Catal.*, 2020, **10**(17), 10169–10184.

62 D. T. Bregante, N. E. Thornburg, J. M. Notestein and D. W. Flaherty, Consequences of Confinement for Alkene Epoxidation with Hydrogen Peroxide on Highly Dispersed Group 4 and 5 Metal Oxide Catalysts, *ACS Catal.*, 2018, **8**(4), 2995–3010.

63 D. T. Bregante, J. Z. Tan, A. Sutrisno and D. W. Flaherty, Heteroatom substituted zeolite FAU with ultralow Al contents for liquid-phase oxidation catalysis, *Catal. Sci. Technol.*, 2020, **10**(3), 635–647.

64 R. A. Yang and M. L. Sarazen, Mechanistic Impacts of Metal Site and Solvent Identities for Alkene Oxidation over Carboxylate Fe and Cr Metal–Organic Frameworks, *ACS Catal.*, 2022, 14476–14491.

65 C. W. Yoon, K. F. Hirsekorn, M. L. Neidig, X. Yang and T. D. Tilley, Mechanism of the Decomposition of Aqueous Hydrogen Peroxide over Heterogeneous TiSBA15 and TS-1 Selective Oxidation Catalysts: Insights from Spectroscopic and Density Functional Theory Studies, *ACS Catal.*, 2011, **1**(12), 1665–1678.

66 R. L. Brutchey, D. A. Ruddy, L. K. Andersen and T. D. Tilley, Influence of Surface Modification of Ti-SBA15 Catalysts on the Epoxidation Mechanism for Cyclohexene with Aqueous Hydrogen Peroxide, *Langmuir*, 2005, **21**(21), 9576–9583.

67 R. R. Sever and T. W. Root, DFT Study of Solvent Coordination Effects on Titanium-Based Epoxidation Catalysts. Part One: Formation of the Titanium Hydroperoxo Intermediate, *J. Phys. Chem. B*, 2003, **107**(17), 4080–4089.

68 M. Neurock and L. E. Manzer, Theoretical insights on the mechanism of alkene epoxidation by H₂O₂ with titanium silicalite, *Chem. Commun.*, 1996, **10**, 1133–1134.

69 F. Bonino, A. Damin, G. Ricchiardi, M. Ricci, G. Spanò, R. D'Aloisio, A. Zecchina, C. Lamberti, C. Prestipino and S. Bordiga, Ti-Peroxo Species in the TS-1/H₂O₂/H₂O System, *J. Phys. Chem. B*, 2004, **108**(11), 3573–3583.

70 N. S. Antonova, J. J. Carbó, U. Kortz, O. A. Kholdeeva and J. M. Poblet, Mechanistic Insights into Alkene Epoxidation with H₂O₂ by Ti- and other TM-Containing Polyoxometalates: Role of the Metal Nature and

Coordination Environment, *J. Am. Chem. Soc.*, 2010, **132**(21), 7488–7497.

71 M. G. Clerici and P. Ingallina, Epoxidation of Lower Olefins with Hydrogen Peroxide and Titanium Silicalite, *J. Catal.*, 1993, **140**, 71–83.

72 J. J. Bravo-Suárez, K. K. Bando, J. Lu, M. Haruta, T. Fujitani and T. Oyama, Transient Technique for Identification of True Reaction Intermediates: Hydroperoxide Species in Propylene Epoxidation on Gold/Titanosilicate Catalysts by X-ray Absorption Fine Structure Spectroscopy, *J. Phys. Chem. C*, 2008, **112**(4), 1115–1123.

73 Y. Yu, Z. Tang, J. Wang, R. Wang, Z. Chen, H. Liu, K. Shen, X. Huang, Y. Liu and M. He, Insights into the efficiency of hydrogen peroxide utilization over titanosilicate/H_2O_2 systems, *J. Catal.*, 2020, **381**, 96–107.

74 N. Morlanes and J. M. Notestein, Kinetic study of cyclooctene epoxidation with aqueous hydrogen peroxide over silica-supported calixarene–Ta (V), *Appl. Catal., A*, 2010, **387**(1–2), 45–54.

75 D. T. Bregante, P. Priyadarshini and D. W. Flaherty, Kinetic and spectroscopic evidence for reaction pathways and intermediates for olefin epoxidation on Nb in* BEA, *J. Catal.*, 2017, **348**, 75–89.

76 M. A. Mellmer, C. Sanpitakseree, B. Demir, P. Bai, K. Ma, M. Neurock and J. A. Dumesic, Solvent-enabled control of reactivity for liquid-phase reactions of biomass-derived compounds, *Nat. Catal.*, 2018, **1**(3), 199–207.

77 M. A. Mellmer, C. Sanpitakseree, B. Demir, K. Ma, W. A. Elliott, P. Bai, R. L. Johnson, T. W. Walker, B. H. Shanks, R. M. Rioux, M. Neurock and J. A. Dumesic, Effects of chloride ions in acid-catalyzed biomass dehydration reactions in polar aprotic solvents, *Nat. Commun.*, 2019, **10**(1), 1132.

78 A. K. Chew, T. W. Walker, Z. Shen, B. Demir, L. Witteman, J. Euclide, G. W. Huber, J. A. Dumesic and R. C. Van Lehn, Effect of Mixed-Solvent Environments on the Selectivity of Acid-Catalyzed Dehydration Reactions, *ACS Catal.*, 2019, **10**(3), 1679–1691.

79 L. Qi, R. Alamillo, W. A. Elliott, A. Andersen, D. W. Hoyt, E. D. Walter, K. S. Han, N. M. Washton, R. M. Rioux, J. A. Dumesic and S. L. Scott, Operando Solid-State NMR Observation of Solvent-Mediated Adsorption-Reaction of Carbohydrates in Zeolites, *ACS Catal.*, 2017, 3489–3500.

80 M. J. Cordon, J. N. Hall, J. W. Harris, J. S. Bates, S.-J. Hwang and R. Gounder, Deactivation of Sn-Beta zeolites caused by structural transformation of hydrophobic to hydrophilic micropores during aqueous-phase glucose isomerization, *Catal. Sci. Technol.*, 2019, **9**(7), 1654–1668.

81 J. C. Vega-Vila and R. Gounder, Quantification of Intraporous Hydrophilic Binding Sites in Lewis Acid Zeolites and Consequences for Sugar Isomerization Catalysis, *ACS Catal.*, 2020, **10**(20), 12197–12211.

82 N. Pfriem, P. H. Hintermeier, S. Eckstein, S. Kim, Q. Liu, H. Shi, L. Milakovic, Y. Liu, G. L. Haller, E. Baráth, Y. Liu and J. A. Lercher, Role of the ionic environment in enhancing the activity of reacting molecules in zeolite pores, *Science*, 2021, **372**, 952–957.

83 F. Chen, M. Shetty, M. Wang, H. Shi, Y. Liu, D. M. Camaioni, O. Y. Gutiérrez and J. A. Lercher, Differences in Mechanism and Rate of Zeolite-Catalyzed Cyclohexanol Dehydration in Apolar and Aqueous Phase, *ACS Catal.*, 2021, **11**(5), 2879–2888.

84 H. Shi, S. Eckstein, A. Vjunov, D. M. Camaioni and J. A. Lercher, Tailoring nanoscopic confines to maximize catalytic activity of hydronium ions, *Nat. Commun.*, 2017, **8**(1), 15442.

85 Y. Liu, A. Vjunov, H. Shi, S. Eckstein, D. M. Camaioni, D. Mei, E. Baráth and J. A. Lercher, Enhancing the catalytic activity of hydronium ions through constrained environments, *Nat. Commun.*, 2017, **8**(1), 14113.

86 J. S. Bates, B. C. Bukowski, J. Greeley and R. Gounder, Structure and solvation of confined water and water–ethanol clusters within microporous Brønsted acids and their effects on ethanol dehydration catalysis, *Chem. Sci.*, 2020, **11**(27), 7102–7122.

87 M. C. Allen, A. J. Hoffman, T.-W. Liu, M. S. Webber, D. Hibbitts and T. J. Schwartz, Highly Selective Cross-Etherification of 5-Hydroxymethylfurfural with Ethanol, *ACS Catal.*, 2020, **10**(12), 6771–6785.

88 R. F. Dejaco, P. Bai, M. Tsapatsis and J. I. Siepmann, Adsorptive Separation of 1-Butanol from Aqueous Solutions Using MFI- and FER-Type Zeolite Frameworks: A Monte Carlo Study, *Langmuir*, 2016, **32**(8), 2093–2101.

89 P. Bai, M. Tsapatsis and J. I. Siepmann, Multicomponent Adsorption of Alcohols onto Silicalite-1 from Aqueous Solution: Isotherms, Structural Analysis, and Assessment of Ideal Adsorbed Solution Theory, *Langmuir*, 2012, **28**(44), 15566–15576.

90 K. Zhang, R. P. Lively, J. D. Noel, M. E. Dose, B. A. McCool, R. R. Chance and W. J. Koros, Adsorption of Water and Ethanol in MFI-Type Zeolites, *Langmuir*, 2012, **28**(23), 8664–8673.

91 R. F. Dejaco, M. Dorneles De Mello, H. G. T. Nguyen, M. Y. Jeon, R. D. Zee, M. Tsapatsis and J. I. Siepmann, Vapor- and liquid-phase adsorption of alcohol and water in silicalite-1 synthesized in fluoride media, *AIChE J.*, 2020, **66**(4), e16868.

92 S. Pahari, M. Dorneles De Mello, M. S. Shah, T. R. Josephson, L. Ren, H. G. T. Nguyen, R. D. Van Zee, M. Tsapatsis and J. I. Siepmann, Ethanol and Water Adsorption in Conventional and Hierarchical All-Silica MFI Zeolites, *ACS Phys. Chem. Au*, 2021, **2**(2), 79–88.

93 D. Shah, K. Kissick, A. Ghorpade, R. Hannah and D. Bhattacharyya, Pervaporation of alcohol–water and dimethylformamide–water mixtures using hydrophilic zeolite NaA membranes: mechanisms and experimental results, *J. Membr. Sci.*, 2000, **179**(1–2), 185–205.

94 Y. Oumi, A. Miyajima, J. Miyamoto and T. Sano, Binary mixture adsorption of water and ethanol on silicalite, in *Studies in Surface Science and Catalysis*, Elsevier, 2002, vol. 142, pp. 1595–1602.

95 H. Ahn, H. Lee, S.-B. Lee and Y. Lee, Pervaporation of an aqueous ethanol solution through hydrophilic zeolite membranes, *Desalination*, 2006, **193**(1–3), 244–251.

96 T. Sano, S. Ejiri, K. Yamada, Y. Kawakami and H. Yanagishita, Separation of acetic acid-water mixtures by pervaporation through silicalite membrane, *J. Membr. Sci.*, 1997, **123**(2), 225–233.

97 M. G. Ahunbay, Monte Carlo Simulation of Water Adsorption in Hydrophobic MFI Zeolites with Hydrophilic Sites, *Langmuir*, 2011, **27**(8), 4986–4993.

98 T. Humplik, R. Raj, S. C. Maroo, T. Laoui and E. N. Wang, Effect of hydrophilic defects on water transport in MFI zeolites, *Langmuir*, 2014, **30**(22), 6446–6453.

99 R. P. Bell, The theory of reactions involving proton transfers, *Proc. R. Soc. London, Ser. A*, 1936, **154**(882), 414–429.

100 M. Evans and M. Polanyi, Further considerations on the thermodynamics of chemical equilibria and reaction rates, *Trans. Faraday Soc.*, 1936, **32**, 1333–1360.

101 J. Brønsted and K. Pedersen, Stöchiometrie und verwandtschaftslehre, *Z. Phys. Chem.*, 1924, **108**, 185–235.

102 G. S. Hammond, A Correlation of Reaction Rates, *J. Am. Chem. Soc.*, 1955, **77**(2), 334–338.

103 E. V. Anslyn and D. A. Dougherty, *Modern Physical Organic Chemistry*, University Science, 2005, pp. 374–377.

104 M. Alvear, K. Eränen, D. Y. Murzin and T. Salmi, Study of the Product Distribution in the Epoxidation of Propylene over TS-1 Catalyst in a Trickle-Bed Reactor, *Ind. Eng. Chem. Res.*, 2021, **60**(6), 2430–2438.

105 G. Wu, Y. Wang, L. Wang, W. Feng, H. Shi, Y. Lin, T. Zhang, X. Jin, S. Wang and X. Wu, Epoxidation of propylene with H2O2 catalyzed by supported TS-1 catalyst in a fixed-bed reactor: experiments and kinetics, *Chem. Eng. J.*, 2013, **215**, 306–314.

106 L. Zhang, K. Chen, B. Chen, J. L. White and D. E. Resasco, Factors that Determine Zeolite Stability in Hot Liquid Water, *J. Am. Chem. Soc.*, 2015, **137**(36), 11810–11819.

107 C. J. Heard, L. Grajciar, F. Uhlík, M. Shamzhy, M. Opanasenko, J. Čejka and P. Nachtigall, Zeolite (in) stability under aqueous or steaming conditions, *Adv. Mater.*, 2020, **32**(44), 2003264.

108 D. E. Resasco, S. P. Crossley, B. Wang and J. L. White, Interaction of water with zeolites: a review, *Catal. Rev.: Sci. Eng.*, 2021, **63**(2), 302–362.